

https://dspace.org/

Event categorization for narrow-width resonance searches in the HZZ4l channel with the ATLAS detector

Thabede, Mzwandile

2020
https://hdl.handle.net/10539/31070

Downloaded from a DSpace repository. https://dspace.org/

Event categorization for narrow-width resonance searches in the $H \to ZZ \to 4\ell$ channel with the ATLAS detector

Author: Mzwandile Thabede
Supervisor: Prof. Bruce Mellado
Co-Supervisor: Dr. Xifeng Ruan



School of Physics
University of the Witwatersrand

A dissertation submitted to the Faculty of Science, University of the Witwatersrand, Johannesburg, in fulfilment of the requirements for the degree of Master of Science.

October 12, 2020

Declaration

I declare that the work in this dissertation is my own and I have not submitted it at any other institution for a degree. The dissertation forms part of the following papers:

- Search for heavy ZZ resonances in the $\ell^+\ell^-\ell^+\ell^-$ final state using proton-proton collisions at $\sqrt{s} = 13$ TeV with the ATLAS detector. **ATL-COM-PHYS-2018-1042** [1]. **Contributions**: High Mass Studies.

- Search for heavy ZZ resonances in the $\ell^+\ell^-\ell^+\ell^-$ final state using proton-proton collisions in 2015-18 at $\sqrt{s} = 13$ TeV with the ATLAS detector. **ATL-COM-PHYS-2018-1697** [2].
  Contributions: Side band Monte Carlo and Data comparisons and cut-based VBF Categorization.

- The ATLAS H4l Analysis Framework and the baseline analysis for the $H \to ZZ \to 4\ell$ channel. **High Energy Particle Physics Workshop 2018, Proceedings:** To appear in the book of proceedings of 2018 [3].
  Contributions: Analysis.

- High mass VBF Categorization for Narrow-width Resonance searches in the $H \to ZZ \to 4\ell$ channel with the ATLAS detector. **South African Institute of Physics 2019, Conference Proceedings:** Accepted for publication [4].
  Contributions: Analysis and text.



Mzwandile E Thabede
October 12, 2020

Abstract

The Higgs boson, which was discovered in 2012 by the ATLAS and CMS collaborations at the LHC, was the first scalar boson (elementary particle of spin zero) to be discovered in nature. This was the last missing piece of the Standard Model and its announcement marked an important milestone in particle physics research. Since then there has been much work done to measure the properties of the Higgs boson as well as to search for new physics beyond the Standard Model. A model was developed in 2015 to understand several features that were initially observed in ATLAS and CMS Run 1 data. This model predicts the existence of a heavy scalar boson with mass estimated around 270 GeV. Heavy scalar bosons considered here are produced mainly via the gluon fusion (ggF) and the vector boson fusion (VBF) production mechanisms. This means the search for these particles can be done in either of these production modes, provided that a method to separate ggF events from VBF events has been clearly defined. It is the scope of this dissertation to categorize signal events in the $H \to ZZ \to 4\ell$ channel into ggF and VBF categories using a cut-based method and ATLAS Monte Carlo with the total integrated luminosity of 140 fb^{-1}. The method based on the signal selection efficiency and background rejection is used to separate ggF events from VBF events by taking advantage of the distinctive 2-jet signature of events in the VBF category. The VBF and ggF production samples with resonant masses from $m_H = 200$ GeV to $m_H = 1000$ GeV were used to optimize the di-jet invariant mass (m_{jj}) and the pseudo-rapidity difference ($\Delta\eta_{jj}$) cuts. The new optimal VBF selection cuts, as obtained in chapter five, require events that satisfy $m_{jj} \geq 450$ GeV and $\Delta\eta_{jj} \geq 3.0$ in order to be classified into the VBF category. Comparison of this new selection with the currently used VBF selection cuts ($m_{jj} \geq 400$ GeV and $\Delta\eta_{jj} \geq 3.3$) shows that the current standard selection is still good enough to be used for cut-based event categorization in the $H \to ZZ \to 4\ell$ channel.

To my mother...

Acknowledgements

I would like to express my gratitudes to my supervisor, Prof. Bruce Mellado for all the opportunities he afforded me to work on my dissertation at CERN. This allowed to make my contributions while learning from experts in the field and at the forefront of particle physics research. His expertise in the subject combined with assistance and encouragement ensured that my time as a MSc student is the most memorable.

I would also like to thank especially, Dr. Theodota Laugori for all her assistance during my studies which include introducing me to the $H \rightarrow ZZ$ Higgs working group at CERN. Her technical guidance and advice in all matters to do with my research has been truly invaluable.

Encouragement and constant reminders during the documentation of this dissertation from a friend and fellow student, Esra, is also highly appreciated. My gratitudes also to Mampionona Rajaoferason for bringing me up to speed with the analysis and all matters to do with the ATLAS Analysis Framework when I joined the collaboration in 2018.

I would like to acknowledge the assistance from SA-CERN and IThemba Labs who sponsored all my trips to CERN, conferences and work shops throughout South Africa and abroad. Their assistance made the completion of this research possible and it made all my travel and stay overseas comfortable and this is truly appreciated.

Last but not least, my gratitude go to my girlfriend and to the rest of my family for all their love and support even when I was uncharacteristically, away from home for long periods of time.

Contents

Declaration i

Abstract ii

Acknowledgements v

List of Figures ix

List of Tables xii

Nomenclature xiii

1 Introduction 2

2 Theoretical Background 4

2.1 Elementary Particles 4

2.1.1 Fermions 5

2.1.2 Bosons 6

2.2 Fundamental Interactions 7

2.3 The Higgs Boson 7

2.4 Brout-Englert-Higgs mechanism 7

2.4.1 The Complex Doublet Field 10

2.4.2 Higgs Boson Production and Decays 11

2.5 The Madala Hypothesis 13

2.6 Summary 18

3 The LHC Experiments 20

3.1 The ATLAS Detector 21

3.1.1 The Inner Detector 23

3.1.2 Calorimeters 24

3.1.3 The Muon Spectrometer 25

3.1.4 The Trigger System . . . 26

4 Object Reconstruction and Event Selection 28
4.1 Data and MC Samples . . . 28
4.1.1 Data Samples . . . 28
4.1.2 Signal MC Samples . . . 29
4.1.3 Background MC Samples . . . 29
4.1.4 Main Background . . . 29
4.1.5 Additional Background . . . 30
4.2 Signal Production . . . 31
4.3 Object Reconstruction . . . 31
4.3.1 Electrons . . . 32
4.3.2 Muons . . . 32
4.3.3 Jets . . . 32
4.4 Four-lepton Event Selection . . . 33
4.4.1 Quadruplet Selection . . . 33
4.4.2 Isolation and Impact Parameter . . . 33
4.4.3 Overlap Removal . . . 34
4.5 Pile-up . . . 34
4.6 High Mass Parameterization . . . 37
4.6.1 The Signal Model . . . 37
4.6.2 The Background Model . . . 38
4.7 High Mass Acceptance . . . 40
4.8 High Mass Control Region . . . 42

5 Event Categorization for Narrow Resonance Searches 44
5.1 Cut-based Categorization . . . 44
5.1.1 Selection Efficiency . . . 46
5.1.2 Background Rejection (1-ϵ(B)) . . . 47
5.1.3 Product (ϵ(S) $\times$ [1- ϵ(B)]) . . . 48
5.2 Summary of Results . . . 50

6 Conclusions 52

A $A \to ZH$ Signal Optimization Study 55
A.1 The Signal . . . 55
A.2 Data and MC . . . 56
A.3 Optimizing the E_T^{miss} Cut . . . 56

B Event Categorization **59**
B.1 Cut-based Classifier 59
B.2 DNN-based Classifier 62

Bibliography **65**

List of Figures

2.1 The diagram showing all fermions and gauge bosons described in the Standard Model. 5

2.2 Scalar potential as a function of ϕ for (a) positive m^2 and (b) negative m^2. 8

2.3 The potential energy as a function of the field ϕ for negative m^2. . . . 9

2.4 The leading order Feynman diagrams for the (a) ggF, (b) VBF, (c) VH and (d) ttH Higgs boson production mechanisms. 12

2.5 (a) The Higgs boson production cross-sections in the range 80 GeV $\leq m_H \leq$ 1000 GeV and (b) the Branching Ratios for the main decay modes of the Higgs particle at the LHC in the range 80 GeV $\leq m_H \leq$ 1000 GeV. 13

2.6 Feynman diagrams showing some of the decay modes of the heavy scalar boson: (a) $H \to Sh$ and (b) $H \to VV$ where V is either a W or a Z boson. 16

2.7 (a) A scan of the negative log likelihood ratios showing different di-lepton plus b-jets and tri-lepton final states for Run 1 and Run 2 with ATLAS and CMS. The black curve shows the likelihood fit for all individual results combined (see reference [36]). 17

2.8 The local p_0 values for the Run 2 searches in the $H \to 4\ell$ channel by ATLAS and CMS, and the p_0 values for ATLAS search in $H \to \mu\mu$ channel, as a function of the invariant mass of the final state system (see reference [37]). 17

3.1 The schematic diagram of the Large Hadron Collider showing the beam path and the main collision points. 21

3.2 The schematic diagram of the ATLAS detector showing its dimensions and vital detector components. 22

3.3 The ATLAS Inner detector showing vital components used for final state object reconstruction. 22

3.4 The inner detector sketch shows the three components plus the new insertable B-layer (IBL). 23
3.5 The sketch of the ATLAS LAr Calorimeter systems. 24
3.6 The schematic figure of the ATLAS muon spectrometer systems. . . . 26

4.1 Feynman diagrams for the non-resonant ZZ production of four-lepton events through the (a) quark- and (b) gluon-initiated processes. . . . 30
4.2 Feynman diagrams for the reducible background processes showing (a) Z+jets and (b) $t\bar{t}$ production at the LHC energy scale. 30
4.3 The luminosity for the 2015 to 2018 data-taking period in figure (a), and the mean number of interactions per proton bunch crossing in figure (b). 35
4.4 Comparison of mc16a with mc16d using the m_{4l} distribution for the (a) $2\mu 2e$ and (b) 4ℓ final state. 35
4.5 Comparison of the shapes of mc16a with mc16d using the η distribution for the positive charge lepton of the leading Z-boson in the (a) $4e$, (b) 4μ, $2\mu 2e$ and (d) 4ℓ final state. 36
4.6 Example of the fitted $m_{4\ell}$ distribution in the (a) $4e$ final state and (b) 4μ final state for $m_H = 300$ GeV mass point. 38
4.7 A fit to the $qq \to ZZ$ background in the $2\mu 2e$ channel. 39
4.8 A fit to the $gg \to ZZ$ background in the $2\mu 2e$ channel. 39
4.9 High mass Signal Acceptance for each production mode with cut-based categorization. The plots show three ggF categories as well as one VBF category for (a) VBF production and (b) ggF production. . 40
4.10 Comparison of the 2018 data set with mc16e using (a) The transverse momentum of a positive charge lepton in the leading lepton pair and (b) the rapidity of the four-lepton system. 43
4.11 Comparison of 2017 data set with the 2018 data set using (a) four lepton invariant mass and (b) the missing transverse energy. 43

5.1 Two important features used for the selection of VBF signal events. The invariant mass of the two leading jets and $\Delta\eta_{jj}$ defined as $\eta_{j1} - \eta_{j2}$ are shown in (a) and (b) respectively for the $m_H = 300$ GeV mass point. 45
5.2 Signal selection efficiency maps for (a) $m_H = 200$ GeV, (b) $m_H = 300$ GeV, (c) $m_H = 400$ GeV and (d) $m_H = 500$ GeV mass points. 46
5.3 background rejection maps only for the (a) $m_H = 200$ GeV, (b) $m_H = 300$ GeV, (c) $m_H = 400$ GeV and (d) $m_H = 500$ GeV mass points. 47

5.4 ϵ(S) × [1- ϵ(B)] maps for the (a) m_H = 200 GeV, (b) m_H = 300 GeV, (c) m_H = 400 GeV and (d) m_H = 500 GeV mass points. 48
5.5 The ϵ(S)×[1-ϵ(B)] 2D map for all nine mass points (m_H = 200 GeV to m_H = 1000 GeV) and it provides the most optimal selection for all nine samples that were used for event categorization. 49
5.6 Selection efficiency (a) and background rejection (b) as a function of mass of the resonance for the optimal selection in the VBF category. 50

A.1 Data and MC comparison using the distributions for the transverse momentum of the four leptons system p_T^{4l} (left) and the number of jets (right). 56
A.2 Selection efficiency for the $A \to ZH$ signal per final state (a) and the expected significance as a function of the E_T^{miss} cut (b). 57

B.1 Selection efficiency maps for (a) m_H = 600 GeV and (b) m_H = 700 GeV mass points. 59
B.2 Selection efficiency maps for (a) m_H = 800 GeV and (b) m_H = 900 GeV mass points. 60
B.3 background rejection maps for the (a) m_H = 600 GeV and (b) m_H = 700 GeV mass points. 60
B.4 background rejection maps for the (a) m_H = 800 GeV and (b) m_H = 900 GeV mass points. 61
B.5 ϵ(S) × [1- ϵ(B)] maps for the (a) m_H = 600 GeV and (b) m_H = 700 GeV mass points. 61
B.6 ϵ(S) × [1- ϵ(B)] maps for the (a) m_H = 800 GeV and (b) m_H = 900 GeV mass points. 62

List of Tables

2.1 Properties of all quarks and leptons. 5
2.2 List of experimental results that were used to constrain parameters in the Madala hypothesis (see reference [18]). 15
2.3 Some of the main decay modes for all $2HDM + S$ scalars. 16
2.4 A summary of the SM+BSM fit results and the results of their combination as discussed in reference [36]. 16

4.1 $qq \to ZZ$ background yields in the mass range 140 GeV $\leq m_{4\ell} \leq$ 800 GeV. 37
4.2 Signal acceptance for ggF and VBF production modes in the four-lepton channel calculated using all Monte Carlo campaigns. The Acceptance is shown for $m_H = 200$ GeV to $m_H = 500$ GeV resonance mass points. 41
4.3 Signal acceptance for ggF and VBF production modes in the four-lepton channel calculated using all Monte Carlo campaigns. The Acceptance is shown for $m_H = 600$ GeV to $m_H = 900$ GeV resonance mass points. 41
4.4 The number of events for the 2018 data and mc16e samples in the side band [70 GeV, 110 GeV] and [140 GeV, 200 GeV] with 59.9 fb^{-1}. 42

A.1 The number of Signal and background MC events and the expected significance for each value of the E_T^{miss} cut. 57

B.1 Input variables in the VBF-DNN classifier 63
B.2 Input variables in the ggF-DNN classifier 63

Nomenclature

Symbols and Acronyms

ATLAS	A Toroidal LHC AparatuS
BEH	Brout-Englert-Higgs
BSM	Beyond Standard Model
BR	Branching Ratio
CB	Crystal Ball
CMS	Compact Muon Solenoid
CR	Control Region
E_T^{miss}	Missing Transverse Energy
ECAL	Electromagnetic Calorimeter
EWSB	Electroweak Symmetry Breaking
ggF	gluon-gluon Fusion
HCAL	Hadronic Calorimeter
ID	Inner Detector
LO	Leading Order
MC	Monte Carlo
MS	Muon Spectrometer
m_{jj}	di-jet invariant mass
$m_{4\ell}$	four-lepton invariant mass
$m_{\ell\ell}$	di-lepton invariant mass
NLO	Next-to-Leading Order
NNLO	Next-to-Next-to-Leading Order
pp	proton-proton
p_T	Transverse Momentum
QCD	Quantum Chromodynamics
SFOS	Same Flavor Opposite Sign
SM	Standard Model
SR	Signal Region
SUSY	Super symmetry
VBF	Vector Boson Fusion
vev	vacuum expectation value
η	pseudo-rapidity
$2HDM$	Two-Higgs Doublet Model

e	electron
μ	muon
s	strange quark
c	charm quark
τ	tau
d	down quark
u	up quark
ν_e	electron nutrino
ν_μ	muon nutrino
ν_τ	tau nutrino
t	top quark
b	bottom quark
$W^\pm$	W-boson
Z	Z-boson
h	Standard Model higgs boson
H	heavy Higgs boson
g	gluon

Chapter 1

Introduction

The study of elementary particles, their properties and the interactions between them is called particle physics. Three of these interactions (electromagnetic force, weak nuclear force and the strong nuclear force) between elementary particles are described by the exchange of integer spin particles, as explained in chapter 2. Following the announcement in 2012 of the Higgs boson (the last piece of the standard model of particle physics) at the Large Hadron Collider (LHC) by the ATLAS [5] and CMS [6] collaborations, much of the work done has been to perform accurate measurements of its physical properties. These include the measurement of the mass, production cross-sections and decay branching ratios. The ATLAS and CMS collaborations are also involved in the ongoing searches for physics beyond the standard model (BSM). This considers the search for heavy Higgs bosons produced with gluon-gluon fusion (ggF), vector boson fusion (VBF) and several other Higgs boson production mechanisms. Section 2.5 introduces a BSM model called the Madala Hypothesis. The hypothesis was developed in 2015 as an attempt to comprehend several anomalies observed in Run 1 data for final states with multiple leptons. The work presented in this dissertation is part of the heavy Higgs boson searches in the ATLAS experiment. A brief introduction of the standard model, which is given in chapter two, forms part of the theoretical background for heavy boson searches in particle physics, in general, and at the LHC experiments, in particular. This is followed by a brief discussion of the LHC accelerator complex and the ATLAS detector in chapter three. An overview of the $H \to ZZ \to 4\ell$ analysis channel with signal as well as background affecting this analysis channel is given in chapter four.

As it was pointed out earlier, that a heavy Higgs boson is produced from gluon fusion and vector boson fusion production mechanisms, it is necessary to distinguish events from each production mode by defining a set of selection requirements (criteria) to be applied on all events that enter the signal region. Given that the ggF

production mode is the most dominant one at the LHC in terms of the Higgs boson production cross-section, one may ask if the sensitivity of the VBF production mode can be improved using Run 2 Monte Carlo from the ATLAS detector. This dissertation attempts to answer this question by adopting a categorization method, which is based on the signal selection efficiency and background rejection maps. The selection for the signal events is based on the characteristic 2-jet signature of the VBF events and this is an important feature that is used to distinguish between ggF and VBF categories. Details of this selection and optimization study is discussed in chapter five where we have assumed the production of a narrow-width resonance (NWA) and the branching ratios for $H \to ZZ$ heavy resonance decays.

Chapter 2

Theoretical Background

The study of elementary particles and the forces by which they interact is called particle physics. These fundamental interactions between elementary particles are described in the Standard Model, as introduced in section 2.2. A brief introduction of the Standard Model is provided in this chapter as motivation for the research study that is being performed. Since the Higgs boson was discovered in 2012, searches for physics beyond the Standard Model have been carried out using different models, such as the Madala Hypothesis. This chapter is intended to provide sufficient introduction to the Standard Model and the role of the Higgs boson in our understanding of the nature of elementary particles and all matter in the universe. Section 2.5 introduces the Madala Hypothesis which aims to explain a number of features observed in Run 1 and Run 2 data from ATLAS and CMS experiments at the LHC.

2.1 Elementary Particles

The Standard Model of particle physics is a model that describes the elementary particles and three of the four fundamental interactions (weak nuclear force, strong nuclear force and electromagnetic force) in nature. The predictions of the Standard Model provide explanation about how matter acquire its mass through spontaneous breaking of the electroweak symmetry. In this section, a brief introduction of the Standard Model of particles, fundamental interactions, the BEH mechanism and how $W^{\pm}$ and Z bosons acquire mass through interaction with the scalar field is provided. A summary of the Higgs boson production mechanisms and decay modes is also provided. Figure 2.1 shows all elementary particles of the Standard Model plus one proposed gravitational force carrier (graviton). The properties (mass and elementary charge) of leptons and quarks are shown in table 2.1. Each of the group of particles (fermions and bosons) are described in section 2.1.1 and section 2.1.2.

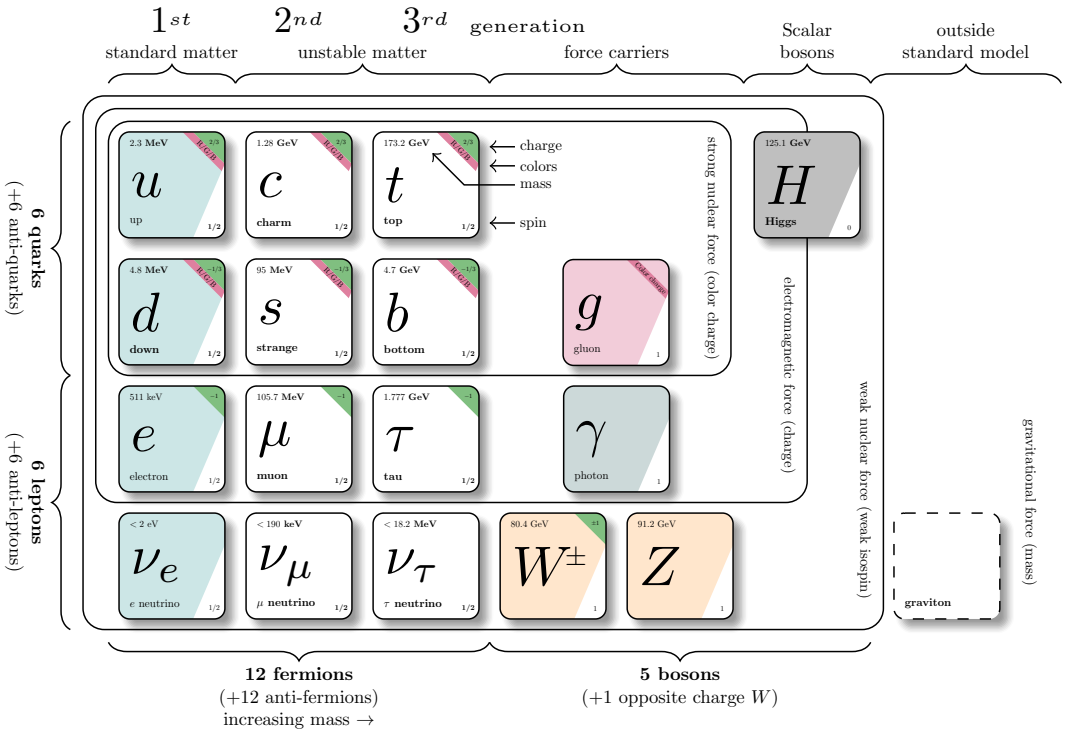

Figure 2.1: The diagram showing all fermions and gauge bosons described in the Standard Model.

Table 2.1: Properties of all quarks and leptons.

Quarks			**Leptons**			
Flavour	Charge	Mass [GeV]	Flavour	Charge	Mass [GEV]	Generation
u	2/3	2.2×10^{-3}	e	-1	5.1×10^{-4}	1st
d	-1/3	4.7×10^{-3}	ν_e	0	$<2\times10^{-9}$	
c	2/3	1.280	μ	-1	0.106	2nd
s	-1/3	9.6×10^{-2}	ν_μ	0	$<1.9\times10^{-4}$	
t	2/3	173.2	τ	-1	1.778	3rd
b	-1/3	4.7	ν_τ	0	$<1.8\times10^{-2}$	

2.1.1 Fermions

Fermions are all elementary particles with one half spin values (particle spin $= \frac{1}{2}$). All Fermions obey Pauli's Exclusion Principle [7], which states that no two particles with the same spin quantum number may occupy the same quantum state. There are two groups of fermions called leptons and quarks. Leptons consist of electron (e), muon (μ), tau (τ), electron neutrino (ν_e), muon neutrino (ν_μ), tau neutrino (ν_τ) and

all anti-leptons. Quarks consist of the up quark (u), down quark (d), top quark (t), bottom quark (b), charm quark (c), strange quark (s) and all anti-quarks. Leptons and quarks are divided into three generations according to their mass and stability (life-time). First generation leptons, for example, are lighter and more stable than the second and third generation leptons. First generation quarks are lighter and more stable than the second and third generation quarks. The top quark is the heaviest of all quarks with the mass of approximately 173 GeV [8]. The top quark, charm quark and up quark all share the same fractional positive charge of $+\frac{2}{3}$ and the bottom, strange and down quarks share the same fractional negative charge of $-\frac{1}{3}$. Quarks bind together to form other subatomic particles, for example, protons are made up of two up-quarks and one down-quark (uud) and neutrons are made up of two down-quarks and one up-quark (udd). All fermions are produced by the excitation of the Dirac Field or a Fermion Field (Ψ). This Fermion field is the field which when excited, will give a particle of spin $\frac{1}{2}$ and is well-described by the Dirac equation:

$$i\gamma^{\mu}\partial_{\mu}\Psi - m\Psi = 0, \tag{2.1}$$

where m is the mass of the fermion that is produced or the fermion that is described by the Dirac Equation (equation 2.1). The Standard Model assumes that all fermions (leptons and quarks) have no mass (mass-less), but it can be seen for example, in the BEH mechanism how fermions acquire their mass through interaction with the scalar field (Higgs Field).

2.1.2 Bosons

Bosons are integer spin elementary particles. We distinguish between two types of bosons, Vector bosons and Scalar bosons as explained in this section. Vector bosons are produced by the excitation of the vector field and scalar bosons are produced by the excitation of the scalar field. Vector Bosons (gauge bosons) are elementary particles of spin 1 (particle spin = 1). There are four gauge bosons discovered so far, the gluon g, photon γ, W boson and Z boson. Gluons are responsible for the strong nuclear force which binds quarks together to form hadrons. The photon is the carrier particle for the electromagnetic force. The vector bosons are carriers of the weak nuclear force. Vector bosons are mass-less excitations of the gauge field. We will see later on in this chapter how the vector bosons acquire their masses through Spontaneous Breaking of Electroweak Symmetry. Scalar Bosons are elementary particles of spin 0 (particle spin = 0). There is one scalar boson discovered so far, the Standard Model Higgs boson. They are produced by the excitation

of the scalar field. The Standard Model Higgs boson, for example, is produced by the excitation of the Higgs field and it is this scalar field that interacts with and give mass to all other elementary particles.

2.2 Fundamental Interactions

In this section, three of the four fundamental interactions are introduced. These are the forces that are described by the Standard Model. The interactions between fermions, for example, is by exchanging a spin-1 gauge boson (photon). We say therefore, that photons are mediators of the electromagnetic force. Gluons mediate the strong nuclear force while the vector bosons mediate the weak nuclear force. The gravitational force (the fourth fundamental interaction) is not covered by the Standard Model, it is described in the general theory of relativity [9, 10]. The weak and electromagnetic interactions are unified at high energies and become known as electroweak interaction. The Standard Model is based on the gauge symmetry structure $SU(3)_c \times SU(2)_L \times U(1)_Y$, where c stands for color, L stands for left-hand leptons and Y is the the weak hyper-charge. $SU(3)_c$ is the Quantum Chromodynamics (QCD) part [11, 12] describing the strong nuclear interactions between gluons and quarks. The $SU(2)_L \times U(1)_Y$ part describes the weak and electromagnetic interactions in the electroweak sector.

2.3 The Higgs Boson

The Higgs Boson is the first fundamental scalar boson to be discovered in nature. It was discovered in 2012 by the ATLAS and CMS collaborations at the Large Hadron Collider (LHC) (see references [5-6]). Since then, much work has been done by both ATLAS and CMS to accurately measure the properties (mass, production cross-section, spin parity etc.) of the Higgs boson. Another important work being done is to search for new physics beyond the Standard Model which is the main purpose of this work. Section 2.4 focuses on the brief theory of the Higgs boson, how elementary particles (W-boson, Z-boson and fermions) acquire their mass through Spontaneous Symmetry Breaking as well as the different Higgs boson production and decay modes.

2.4 Brout-Englert-Higgs mechanism

It was pointed out earlier that other elementary particles acquire their mass by interacting with the scalar field (ϕ). This is explained by the Brout-Englert-Higgs (BEH) mechanism [13, 14]. The BEH mechanism describes how matter acquire its mass through spontaneous symmetry breaking (SSB). We start with the singlet field

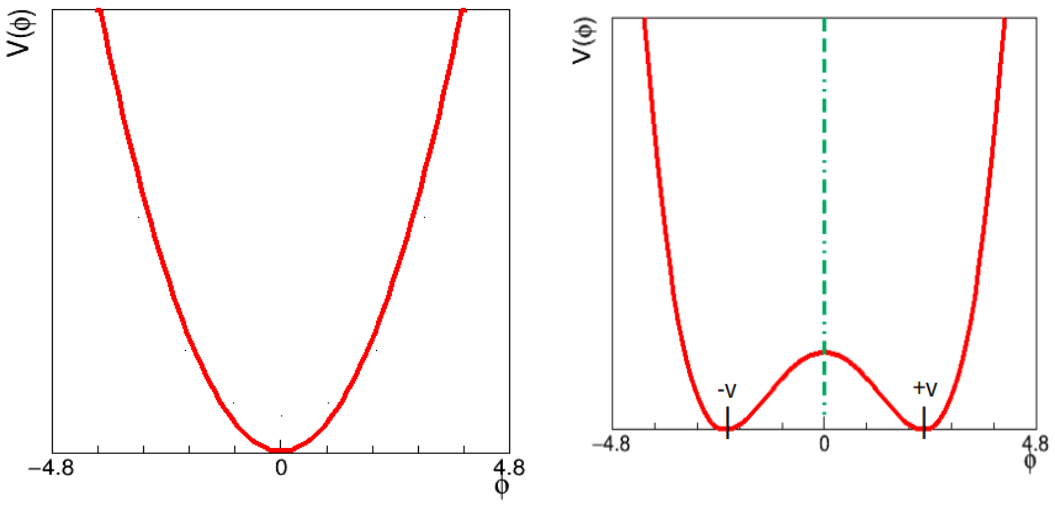

(a) (b)

Figure 2.2: Scalar potential as a function of ϕ for (a) positive m^2 and (b) negative m^2.

and then later on we also look at the doublet field. The Lagrangian of a singlet scalar field can be written as:

$$\mathcal{L} = \frac{1}{2}(\partial_\mu \phi)^2 - (\frac{1}{2}m^2\phi^2 + \frac{1}{4}\lambda\phi^4), \tag{2.2}$$

with the potential energy term given by:

$$V(\phi) = \frac{1}{2}m^2\phi^2 + \frac{1}{4}\lambda\phi^4. \tag{2.3}$$

The mass of particles produced by the excitation of this field is denoted by m. If one takes the m^2 term to be positive ($m^2 > 0$) or in other words, if the mass of the excitation is positive or real, the Lagrangian describes a mass-less vector boson interacting with a massive scalar boson and the graph of the potential against ϕ is a parabola with a minimum at $\phi = 0$ as shown in figure 2.2 (a). If, however, the m^2 term is negative ($m^2 < 0$), the potential has a degenerate set of minima at $\pm v = \pm\sqrt{\frac{-m^2}{\lambda}} \equiv vev$ where vev is the vacuum expectation value, the value of the field that minimizes the potential. Unlike before, the potential now has a maximum at $\phi = 0$ and two minima at $\phi = \pm v$, as shown in figure 2.2 (b). Since m is taken to represent the mass in the Lagrangian, we can say that the mass of particles excited in either of the valleys is given by $m = \sqrt{\lambda v^2}$. We can witness the creation of the Higgs particles and the massless excitation of the scalar field called the Goldstone boson (Higgs particle with zero mass). To see this we write the scalar field in polar form

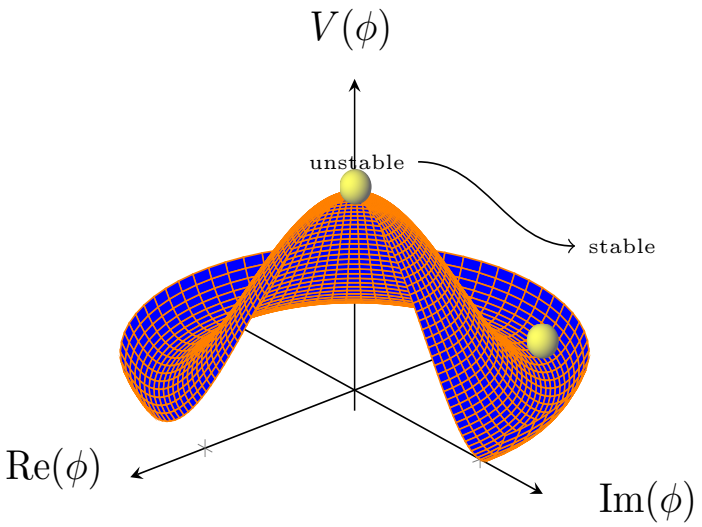

Figure 2.3: The potential energy as a function of the field ϕ for negative m^2.

with radial and angular vibrations at the potential minimum (valley) by substituting $\phi = \rho e^{i\omega}$ and its complex conjugate $\phi^* = \rho e^{-i\omega}$. If we substitute $\phi^2 = \phi\phi^* = \rho^2$ and $m^2 = \text{-}\lambda v^2$ in equation 2.2, we get the the Lagrangian in the form:

$$\begin{aligned}\mathcal{L} &= \frac{1}{2}(\partial\rho^2 + i\rho\partial\rho\partial\omega - i\rho\partial\rho\partial\omega + \rho^2\partial\omega^2) + \frac{1}{2}\lambda v^2\rho^2 - \frac{1}{4}\lambda\rho^2 \\ &= \frac{1}{2}\partial\rho^2 + \frac{1}{2}\lambda v^2\rho^2 + \rho^2\partial\omega^2 - \frac{1}{4}\lambda\rho^4.\end{aligned} \tag{2.4}$$

Since the mass terms are both positive, this is the unstable situation when the field is at the top of the hill and therefore any particle produced at this stage will have imaginary mass. To get stable excitations, we need to shift the zero of the field to coincide with the minimum potential as indicated in figure 2.3. To do this we substitute $\rho = v + h$, which gives the following Lagrangian:

$$\mathcal{L} = \frac{1}{2}(\partial h)^2 - \lambda v^2 h^2 + \frac{1}{2}v^2\partial\omega^2 - \lambda v h^3 - \frac{1}{4}\lambda h^4, \tag{2.5}$$

where h represents the vibration of the field that results in the change in potential energy and ρ is the angular changes of the field from real to imaginary values. We can now afford to lose the higher order self-interaction terms which leaves us with a

more simpler Lagrangian:

$$\mathcal{L} = \frac{1}{2}(\partial h)^2 - \lambda v^2 h^2 + \frac{1}{2} v^2 \partial \omega^2. \tag{2.6}$$

The negative mass term, $-\lambda v^2 h^2$, is evidence that any Higgs particle resulting from the excitation of this field will have real (positive) mass. This is the excitation at any point on the valley in figure 2.3 resulting from the vibration of the field with some changes in potential energy. There is another particle produced by the excitation of this field, the Goldstone particle from the last term ($+\frac{1}{2}v^2\partial\omega^2$). Since the last term is positive and is independent of the radial vibration (h), it means it results from the vibration of the field in the ϕ direction only (without any change in the potential energy) and so the Goldstone particle produced by this oscillation of the field will have zero mass. We get the mass of the Higgs particle by comparing the mass terms from equation 2.3 and equation 2.6 which gives $m_h = \sqrt{2\lambda v^2}$. After spontaneous symmetry breaking, the complex scalar field produces not only the massive Higgs particle, but also the mass-less Goldstone particle.

2.4.1 The Complex Doublet Field

So far we have only considered a scalar singlet field which is why we only get one Goldstone particle and a Higgs particle. To understand the origin of the $W^{\pm}$ and Z boson mass, we need a field structure with more degrees of freedom. The complex doublet field will result in the Higgs particle plus three Goldstone particles which donate the three extra degrees of freedom required for $W^{\pm}$ and Z particles to acquire mass terms. The photon cannot couple to the Higgs field without violating gauge invariance so it remains mass-less, as predicted by the Standard Model. The scalar doublet with four components can be written as:

$$\phi = \begin{pmatrix} \phi^{\dagger} \\ \phi^0 \end{pmatrix} = \frac{1}{\sqrt{2}} \begin{pmatrix} \phi_1 + i\phi_2 \\ \phi_3 + i\phi_4 \end{pmatrix}, \tag{2.7}$$

where $\phi^{\dagger}$ represents a charged field with two components ($\phi_1 + \phi_2$) and ϕ^0 represents a neutral field with two components ($\phi_3 + \phi_4$). The potential energy of the field is given by equation 2.3 and the covariant derivative [15] for the field in the kinetic term can be written as:

$$D_\mu \phi = (\partial_\mu + igT^i W_\mu^i + i\frac{g^{'}}{2} B_\mu)\phi. \tag{2.8}$$

Only the neutral component of the field can acquire the vacuum expectation value so we choose only ϕ^0 and write:

$$\phi^0 = \frac{1}{\sqrt{2}} \begin{pmatrix} 0 \\ v+h \end{pmatrix}. \tag{2.9}$$

To get the $W^{\pm}$ and Z boson masses, we write only the contribution of the gauge boson mass and ignore terms with h

$$(D^{\mu}\phi)^{+}(D_{\mu}\phi) = \frac{1}{8} \left| \begin{pmatrix} gW_{\mu}^{1} - igW_{\mu}^{2} \\ -gW_{\mu}^{3} + g^{'}B_{\mu} \end{pmatrix} \begin{pmatrix} 0 \\ v \end{pmatrix} \right|^2 \tag{2.10}$$

$$(D^{\mu}\phi)^{+}(D_{\mu}\phi) = \frac{v^2}{8}[(gW_{\mu}^{1})^2 + (gW_{\mu}^{2})^2 + (gW_{\mu}^{3} - g^{'}B_{\mu})^2]. \tag{2.11}$$

W_{μ}^{i} is the $SU(2)_L$ gauge boson ($W^{\pm}$ and Z) and B_{μ} is the $U(1)_Y$ gauge boson (γ). This gives the charged gauge boson and its mass as:

$$W_{\mu}^{\pm} = \frac{(W_{\mu}^{1} \pm iW_{\mu}^{2})}{\sqrt{2}}, \tag{2.12}$$

$$m_{W^{\pm}}^{2} = \frac{g^2 v^2}{4}, \tag{2.13}$$

as well as the neutral Z particle and its mass as:

$$Z_{\mu} = \frac{(gW_{\mu}^{3} - g^{'}B_{\mu})}{\sqrt{g^2 + (g^{'})^2}}, \tag{2.14}$$

$$m_Z = \frac{v(g^2 + g^{'2})^{\frac{1}{2}}}{2}. \tag{2.15}$$

If we use a doublet field, we will have three additional degrees of freedom (from three Goldstone particles), one for each gauge boson ($W^{\pm}$ *and* Z) to acquire the mass term. This is the reason why $W^{\pm}$ and Z particles are observed to have have mass in experiments.

2.4.2 Higgs Boson Production and Decays

The production mechanisms for the Higgs boson at the LHC are introduced in this section. The four main production mechanisms according to the size of the production cross-section are: gluon-gluon fusion (ggF), vector boson fusion (VBF), higgstrahlung or vector boson associated production (VH) as well as the top pair associated production (ttH). The leading order Feynman diagrams for Higgs boson production mechanism are shown in figure 2.4. Since the Higgs boson coupling to the top quark is much stronger compared to the other quarks, we consider only top-quark loops in the ggF production mechanism. Figure 2.4 shows only the diagrams

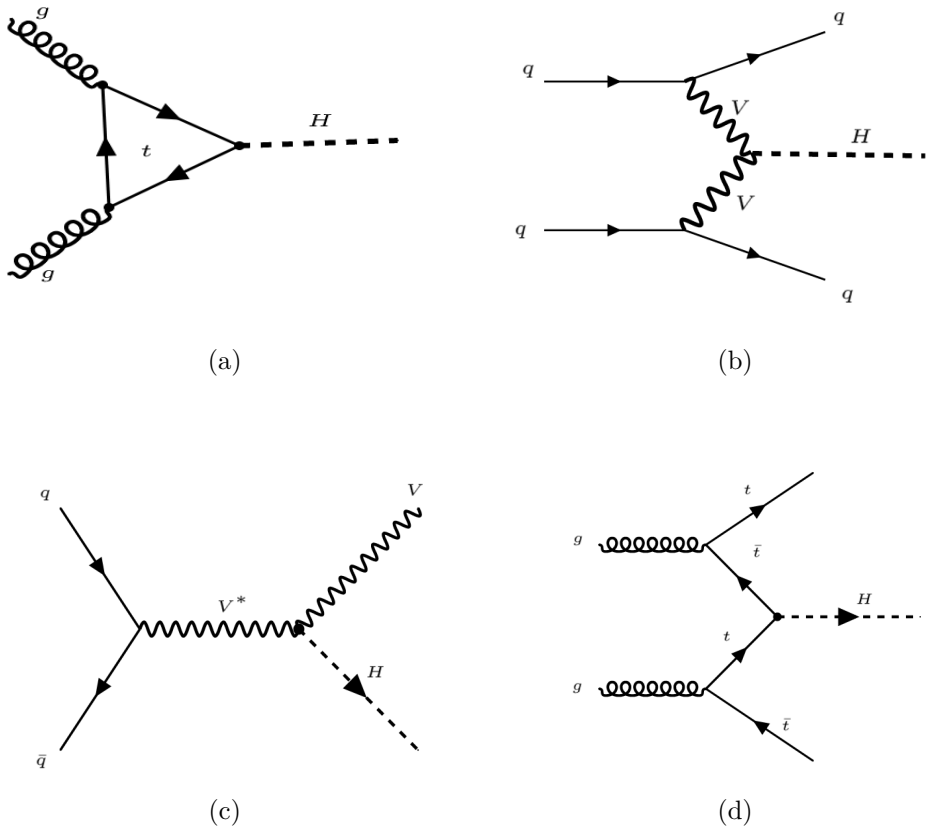

Figure 2.4: The leading order Feynman diagrams for the (a) ggF, (b) VBF, (c) VH and (d) ttH Higgs boson production mechanisms.

for the processes with the most contributions to the total Higgs boson production cross-section at the LHC. The Higgs boson production cross-sections for the main production mechanisms are shown in figure 2.5 (a) [16] and the branching ratios are shown in figure 2.5 (b) [17]. Some of the main decay modes of the Higgs boson are introduced in this section. The Higgs boson is unstable and it decays to other more stable particles immediately after it is produced. The fermionic decay modes involve the decay of the Higgs boson into leptons and quarks. These are: $\mu^+\mu^-$, $\tau^+\tau^-$, $c\bar{c}$ and $b\bar{b}$ decays. The strength of the interaction between the Higgs boson and fermions is proportional to the mass of the fermion. This means the Higgs boson is more likely to decay to heavier fermions, for example, the $b\bar{b}$ decay is more likely to occur than the $\mu^+\mu^-$ decay. The Higgs boson also decays to gauge bosons W^+W^- and ZZ when the mass of the Higgs boson is approximately twice the mass of the top quark ($m_H \geq 2m_t$). The WW decay has the larger branching ratio than the ZZ decay mode. The ZZ decays leptonically to four leptons in the $H \to ZZ \to 4\ell$ ($\ell = \mu$ and e). Although this Higgs boson decay mode has a small branching fraction, it

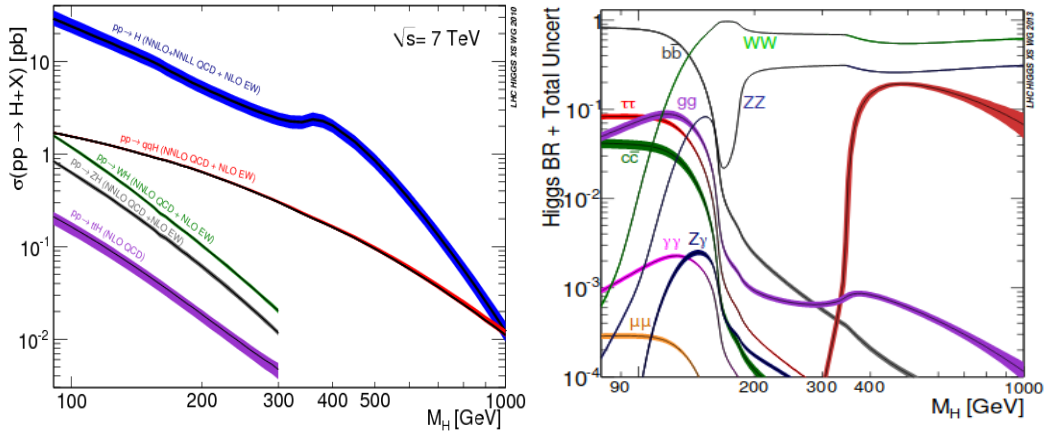

(a) (b)

Figure 2.5: (a) The Higgs boson production cross-sections in the range 80 GeV $\leq m_H \leq$ 1000 GeV and (b) the Branching Ratios for the main decay modes of the Higgs particle at the LHC in the range 80 GeV $\leq m_H \leq$ 1000 GeV.

is easy to reconstruct with small background in the signal region. The Higgs boson also decays to photons and gluons via a heavy quark loop. This is because the Higgs cannot couple directly to the gluon or photon so loop corrections with heavy quarks must be applied.

2.5 The Madala Hypothesis

The Madala hypothesis [18, 19, 20] was developed to search for physics beyond Standard Model (BSM). This hypothesis was formulated in 2015 by colleagues at the Wits Institute for Collider Particle Physics and Harish-Chandra Research Institute (HRI) as an attempt to explain several anomalies observed in Run 1 experimental data from the LHC. This predicts the existence of a heavy scalar (H), named the Madala boson, with mass constrained between ($2\mathrm{m}_h \leq \mathrm{m}_H \leq 2\mathrm{m}_t$). The mass of the heavy scalar is restricted to 2-times the mass of the top-quark due to the increase in the top Yukawa coupling for masses above $2m_t$ and the heavy scalar will decay preferentially to a pair of top-quarks. This was done to explain a distortion observed in the Higgs boson transverse momentum (p_T^h) spectrum and other anomalies. These anomalies in the p_T^h spectrum were first observed in Run 1 data and they still persist in Run 2 data. This distortion in the p_T^h spectrum can be interpreted as an indication for the heavy Higgs particle production and can be seen as a hint for new physics beyond the Standard Model. The Standard Model is extended by adding to the Lagrangian, another term ($\mathcal{L}_{BSM}$) containing BSM interactions:

$$\mathcal{L} = \mathcal{L}_{SM} + \mathcal{L}_{BSM}. \tag{2.16}$$

The BSM term contains the quartic interaction, the Yukawa interaction and the trilinear interaction terms given by:

$$\mathcal{L}_H = -\frac{\beta_g}{4}\kappa^{SM}_{hgg} G_{\mu v} G^{\mu v} H + \beta_v \kappa^{SM}_{hVV} V_\mu V^\mu H, \tag{2.17}$$

$$\mathcal{L}_T = -\frac{v}{2}(\lambda_{Hhh} Hhh), \tag{2.18}$$

$$\mathcal{L}_Q = -\frac{1}{4}\lambda_{HHhh} HHhh, \tag{2.19}$$

$$\mathcal{L}_Y = -\frac{1}{\sqrt{2}}(y_{ttH} t\bar{t}H + y_{bbH} b\bar{b}H). \tag{2.20}$$

The term $\beta_g \kappa^{SM}_{hgg}$ is the coupling strength of H with gluons, $\beta_v \kappa^{SM}_{hVV}$ is the coupling strength of H with vector bosons and $vev = 246$ GeV is the vacuum expectation value which gives mass to the $W^\pm$ and Z bosons after spontaneous EWSB. In the simplified model, a mediator (S) is introduced and it is assumed to be a Higgs-like scalar with mass in the range ($m_h \leq m_S \leq m_H - m_h$). This Higgs-like scalar may decay to vector bosons and lead to a number of leptonic and hadronic final states. The production of S is mainly through the ($H \to Sh$ and $H \to SS$) decay modes of the heavy scalar and the Lagrangian for this interaction can be written as:

$$\begin{aligned}\mathcal{L}_{HhS} = -\frac{v}{2}\,[&\lambda_{hhS} hhS + \lambda_{hSS} hSS + \lambda_{HHS} HHS \\ &+\lambda_{HSS} HSS + \lambda_{HhS} HhS].\end{aligned} \tag{2.21}$$

This gives S the vacuum expectation value. S is given Higgs-like branching ratios by fixing the parameters in the Lagrangian that describes it:

$$\begin{aligned}\mathcal{L}_S = -\frac{\alpha_s \kappa_{Sgg}}{48\pi v} S G^{\alpha\mu v} G^{\alpha}_{\mu v} + \frac{\alpha \kappa_{S\gamma\gamma}}{4\pi v} S F^{\mu v} F_{\mu v} + \frac{\alpha \kappa_{SZZ}}{4\pi v} S Z^{\mu v} Z_{\mu v} \\ + \frac{\alpha \kappa_{SZ\gamma}}{4\pi v} S Z^{\mu v} F_{\mu v} + \frac{\alpha \kappa_{SWW}}{4\pi v} S W^{+\mu v} W^-_{\mu v} \\ - \sum \frac{m_f \kappa_{Sf}}{v} S \bar{f} f.\end{aligned} \tag{2.22}$$

Parameters of the hypothesis are constrained using results from top-pair associated Higgs particle production (ttH), the Higgs boson transverse momentum spectra, di-Higgs boson searches ($H \to hh$) as well as VV ($\mathrm{W}^\pm/Z$) decays. The selection of CMS and ATLAS results that were used to constrain the parameters in the Madala

Table 2.2: List of experimental results that were used to constrain parameters in the Madala hypothesis (see reference [18]).

Results		**Publication**
Differential Higgs boson p_T spectra	ATLAS	Fiducial cross section measurements on $h \to \gamma\gamma$ [21] and $h \to ZZ \to 4l$ [22]
	CMS	Fiducial cross section measurements on $h \to \gamma\gamma$ [23] and $h \to ZZ \to 4l$ [24]
Di-Higgs boson resonance searches	ATLAS	Limits on $H \to hh \to b\bar{b}\tau\tau, \gamma\gamma WW^*$ $\gamma\gamma b\bar{b}$ and $b\bar{b}b\bar{b}$ [25]
	CMC	Limits on $H \to hh \to \gamma\gamma b\bar{b}$ [26], $b\bar{b}\tau\tau$ [27], $\gamma\gamma b\bar{b}$ and multi-leptons [28]
Top-associated Higgs Production	ATLAS	Limits on $h \to \gamma\gamma$ [29], Measurements on multi-lepton channels [30] and $h \to b\bar{b}$ [31]
	CMS	Limits on $h \to \gamma\gamma$ and $h \to b\bar{b}$ [32]
$H \to VV$ decays	ATLAS	Limits on $H \to WW$ [33] and $H \to ZZ$ [34]
	CMS	Limits on $H \to WW$ and $H \to ZZ$ [35]

Hypothesis are shown in table 2.2. Some of the decay modes of the heavy scalar are shown in figure 2.6. Introducing this heavy scalar and a mediator into the 2HDM model leads to five new scalars ($A,\ H,\ h$ and $H^{\pm}$). The six scalars resulting from embedding H and S into the $2HDM$ are shown in table 2.3, each with its possible decay modes for the given mass range.

The scalars presented in table 2.3 with their decay modes increase the number of searches associated with the Madala hypothesis. A is a CP-odd pseudo-scalar with a number of decay modes including $A \to t\bar{t},\ ZH,\ Zh,\ ZS$ and $W^{\pm}H^{\pm}$. The $A \to ZH$ decay mode was optimized using fiducial (truth) mini-trees in events with four leptons and missing transverse energy. This study is summarized in Appendix A. The heavy scalar decays in a number of ways including $H \to Sh,\ H \to hh$ and $H \to SS$ where the Standard Model Higgs boson with mass ($m_h \approx 125$ GeV) is denoted by h and the scalar S decays to $W^{\pm}$ and Z-bosons assuming it has a mass of around 160 GeV. This leads to events with leptons, jets and missing transverse energy.

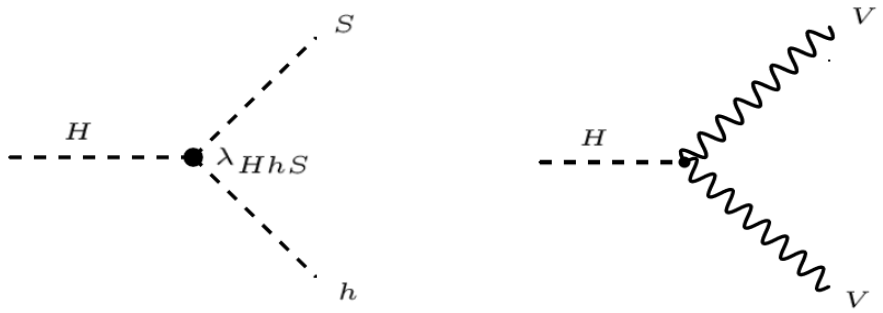

(a) (b)

Figure 2.6: Feynman diagrams showing some of the decay modes of the heavy scalar boson: (a) $H \to Sh$ and (b) $H \to VV$ where V is either a W or a Z boson.

Table 2.3: Some of the main decay modes for all $2HDM + S$ scalars.

Scalar	**Decay Modes**
h	ZZ, W^+W^-, $\gamma\gamma$, $Z\gamma$, $\tau^+\tau^-$, $\mu^+\mu^-$, $c\bar{c}$, gg,$b\bar{b}$
H	ZZ, W^+W^-, SS, Sh, hh, $\gamma\gamma$, $Z\gamma$, $\tau^+\tau^-$, $\mu^+\mu^-$, $c\bar{c}$, gg,$b\bar{b}$
S	ZZ, W^+W^-, $\chi\chi$, $\gamma\gamma$, $Z\gamma$, $\tau^+\tau^-$, $\mu^+\mu^-$, $c\bar{c}$, gg,$b\bar{b}$
$H^{\pm}$	ZZ, W^+W^-, $W^{\pm}h$, $W^{\pm}S$, $W^{\pm}H$, $\gamma\gamma$, $Z\gamma$, $\tau^+\tau^-$, $\mu^+\mu^-$, $c\bar{c}$, gg,$b\bar{b}$
A	ZZ, W^+W^-, Zh, ZH, ZS, $t\bar{t}$, $\gamma\gamma$, $Z\gamma$, $\tau^+\tau^-$, $\mu^+\mu^-$, $c\bar{c}$, gg,$b\bar{b}$

Table 2.4: A summary of the SM+BSM fit results and the results of their combination as discussed in reference [36].

Selection	**Best-fit β_g^2**	**Significance**
ATLAS Run 1 SS ll and $lll + b$-jets	6.51 ± 2.99	2.37σ
ATLAS Run 1 OS $e\mu$+b-jets	4.09 ± 1.37	2.99σ
ATLAS Run 2 SS leptons + b-jets	2.22 ± 1.19	2.01σ
CMS Run 2 SS leptons + b-jets	1.41 ± 0.80	1.75σ
CMS Run 2 OS $e\mu$	2.79 ± 0.52	5.45σ
ATLAS Run 2 SS ll and $lll + b$-jets	5.42 ± 1.28	4.06σ
ATLAS Run 2 tri-lepton + E_T^{miss}	9.05 ± 3.35	2.25σ
CMS Run 2 tri-lepton + E_T^{miss}	9.70 ± 3.88	2.36σ
Combination	2.92 ± 0.35	8.04σ

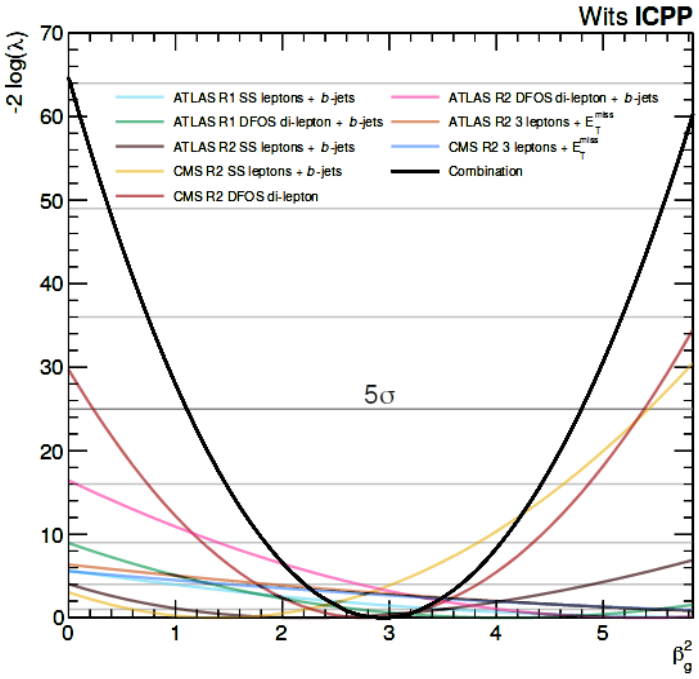

Figure 2.7: (a) A scan of the negative log likelihood ratios showing different di-lepton plus b-jets and tri-lepton final states for Run 1 and Run 2 with ATLAS and CMS. The black curve shows the likelihood fit for all individual results combined (see reference [36]).

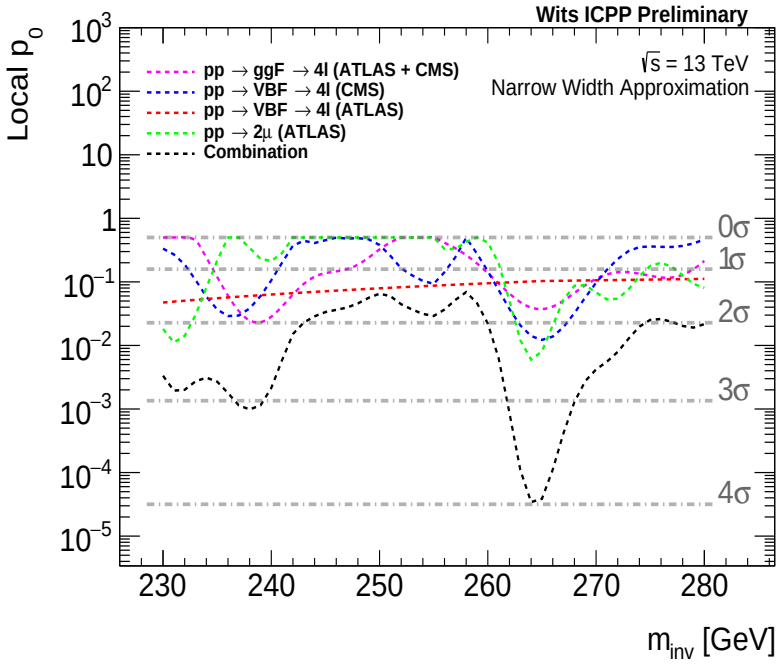

Figure 2.8: The local p_0 values for the Run 2 searches in the $H \to 4\ell$ channel by ATLAS and CMS, and the p_0 values for ATLAS search in $H \to \mu\mu$ channel, as a function of the invariant mass of the final state system (see reference [37]).

Much emphasis is being placed on the multi-lepton final states to try and understand the discrepancies observed in Run 1 and initial Run 2 data. By considering a simplified model where H decays to Sh ($H \rightarrow Sh$) and assuming that S is a Higgs-like scalar in order to reduce the number of parameters, one can try to understand the discrepancies in the data for events leading to multi-lepton final states. This is possible if S is a Higgs-like scalar and decays to a vector-boson pair (WW or ZZ) leading to charged leptons (e and μ) in the final state and h will mostly decay to bottom-quarks. The masses in the model are constrained to $m_H = 270$ GeV and $m_S = 150$ GeV and using only one parameter (β_g^2) for the fit. Several fits for the multi-lepton final state were performed using both ATLAS and CMS data. Fit results for same sign (SS) di-leptons and tri-leptons in association with b-jets and opposite sign (OS) lepton were performed using ATLAS and CMS Run 1 and Run 2 data. The profile likelihood ratio for each multi-lepton final state as well as the combined results (black line) are shown in figure 2.7 and table 2.4 [36]. The fit yields $\beta_g^2 = 2.92 \pm 0.35$ and the upper limit of the significance is $z = 8.04\sigma$ for the SM+BSM hypothesis. The combination is obtained by multiplying the profile likelihood ratios of each measurement. The significance for each fit was calculated as a square root of the y-intercept shown in figure 2.7. This indicates the prospects of BSM searches in the di-lepton plus b-jets and tri-lepton plus missing transverse energy (E_T^{miss}) final states.

Resonant searches in the four lepton decay channel are ongoing both in the ATLAS and CMS collaborations. As it can be seen in figure 2.8 [37], hints from the analysis of incomplete Run 2 data set that there might be excesses in the region of $m_H = 250$ GeV to $m_H = 280$ GeV. This figure shows the local p_0 values drawn as a function of the invariant mass of the final state leptons for the narrow-width resonance in the ggF and VBF production modes. One can interpret these excesses as a hint for physics beyond the Standard Model (BSM) in events with multiple leptons in the final state. This is a good motivation for heavy boson searches in the $H \rightarrow ZZ \rightarrow 4l$ analysis channel using full Run 2 data and in the future of the LHC.

2.6 Summary

The success of the Standard Model of elementary particles is unprecedented. All particles predicted by the model have already been confirmed in experiments. This is after the last missing piece (the Higgs boson) was discovered in 2012 after many years of searching. Much of the work going on since the Higgs boson was discovered have been to perform accurate measurements of its properties and to

search for heavier cousins of the Higgs boson that may shed more light into our understanding of the universe. Although the Standard Model is a successful theory, there are still many unanswered questions. It cannot, for example, explain the origin of dark matter and dark energy, which constitute the largest part of the mass-energy budget in the universe, the matter-antimatter asymmetry in the universe and it also failed to quantize the fourth fundamental force (gravity) for elementary particles. Parts of this has prompted the development of new theories that specifically search for physics beyond the Standard Model.

In this chapter, two families of elementary particles called fermions and bosons were described. We have seen that fermions are elementary particles with half integer spins and are divided into two groups, leptons and quarks. Bosons are elementary particles with integer spins. We introduced gauge bosons (particles with spin equal to one) and scalar bosons (particles with spin equal to zero). Three of the four fundamental interactions of nature were also introduced and the Higgs mechanism and how it explains the acquisition of mass for the $W^{\pm}$ and Z bosons through spontaneous breaking of electroweak symmetry. The production mechanisms and decay modes of the Higgs boson at the LHC were also introduced as well as the searches for new physics beyond Standard Model was also touched upon by looking at a brief introduction of the Madala Hypothesis.

Chapter 3

The LHC Experiments

The Large Hadron Collider (LHC) is the largest particle accelerator in the world. The LHC hosts four main experiments (ATLAS, CMS, ALICE and LHCb) positioned at various points on the 27 km long accelerator. The LHC was designed with two most important parameters, the maximum energy of the colliding proton bunches and the luminosity. The Linear accelerator strips away electrons from hydrogen atoms and feeds all the resulting protons into the Proton Synchrotron Booster. The beam of protons starts from the linear accelerator (LINAC2) all the way to the Super Proton Synchrotron (SPS) before being injected into the LHC ring at the energy of 450 GeV. At this point, the beam is split into two separate beams in two opposite directions. The current LHC machine then accelerates protons, steering them into a circular path using dipole magnets until they reach the center of mass energy of about 13 TeV. The instantaneous luminosity is proportional to the total number of protons in the colliding bunches as well as the number of colliding bunches. Integrated over a period of time for data taking, this results in what is known as the integrated luminosity. The integrated luminosity relates the number of events to the production cross-section for a particular process:

$$N = L \times \sigma. \tag{3.1}$$

This means the total luminosity of the LHC machine needs to be known in order to accurately estimate the number of events for different production mechanisms.

The LHC has two general purpose detectors (ATLAS and CMS) which are used mainly to discover and measure the properties of the Higgs boson and to search for new physics beyond the standard model. In this section, a brief overview of the ATLAS detector is provided, focusing on the detector systems and components that are needed to reconstruct a variety of final state objects.

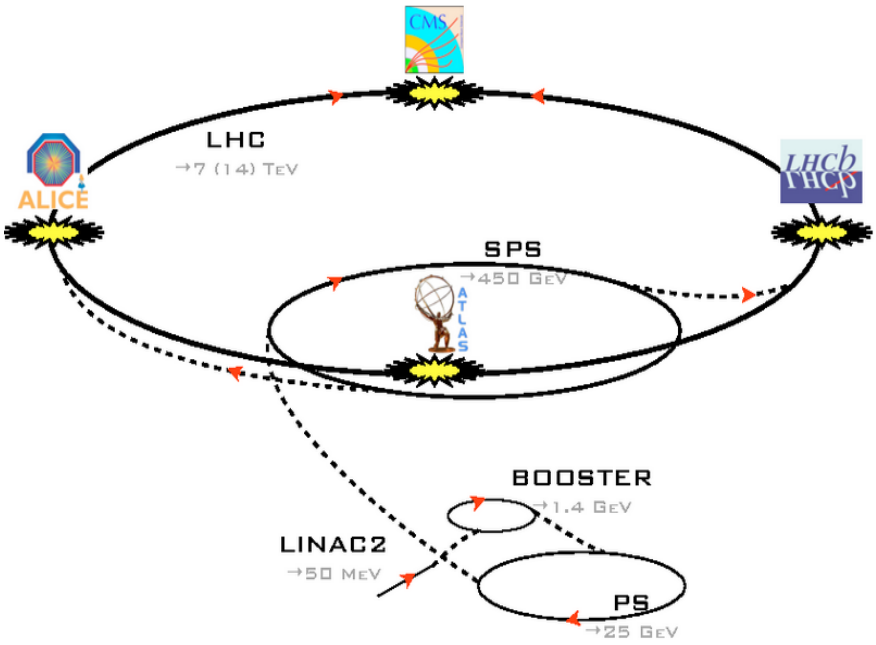

Figure 3.1: The schematic diagram of the Large Hadron Collider showing the beam path and the main collision points.

3.1 The ATLAS Detector

A Toroidal LHC ApparatuS (ATLAS) is one of two general purpose detectors installed at the LHC that was used for the search and discovery of the Standard Model Higgs boson in 2012 (see reference [5-6]). The ATLAS detector components and their uses are discussed in this section. The ATLAS detector weighs approximately 7000 000 kilograms with the dimensions of 44 m in length and 25 m in height. The different detector components are the Inner Detector (ID), the Calorimeters (Electromagnetic Calorimeter and Hadronic Calorimeter), as well as the Muon Detector (muon spectrometer). The sketch diagram of the ATLAS detector is shown in figure 3.2 [38]. ATLAS is designed with the positive z-axis in the direction of the beam pipe, the positive y-axis is upwards towards the surface and the positive x-axis towards the center of the LHC ring. Cylindrical coordinates (r, ϕ, η) are used where η is the pseudo-rapidity given by:

$$\eta = -\ln\left[\tan\left(\frac{\theta}{2}\right)\right]. \tag{3.2}$$

For massive objects such as jets, the rapidity (y) is used instead, and is defined as:

$$y = \frac{1}{2}\ln\left(\frac{E + p_Z}{E - p_Z}\right). \tag{3.3}$$

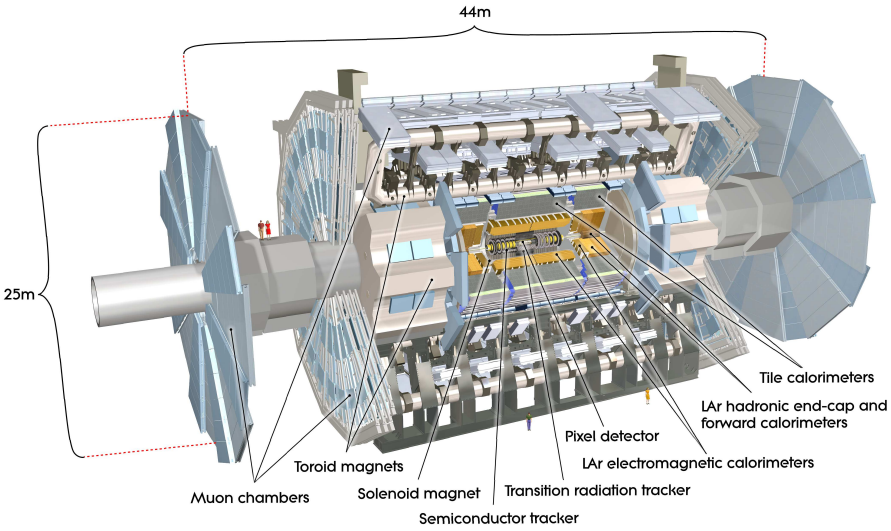

Figure 3.2: The schematic diagram of the ATLAS detector showing its dimensions and vital detector components.

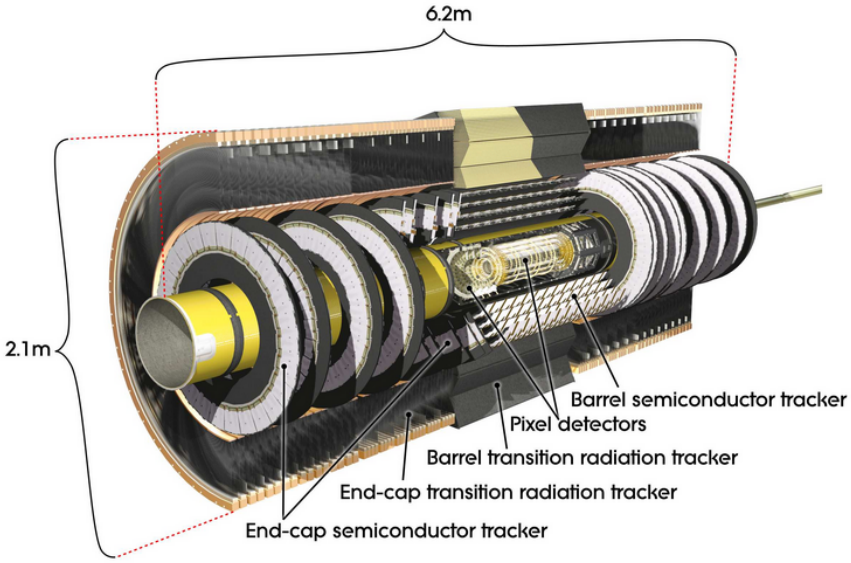

Figure 3.3: The ATLAS Inner detector showing vital components used for final state object reconstruction.

The angular separation between two particle tracks is expressed in terms of ΔR and defined as $\Delta R = \sqrt{\Delta\eta^2 + \Delta\phi^2}$. All ATLAS systems are arranged in concentric cylinders wrapped around the beam pipe with the end caps arranged perpendicular to the beam pipe. This arrangement of detector systems around the interaction point ensures that the detector covers a solid angle of almost 4π steradian.

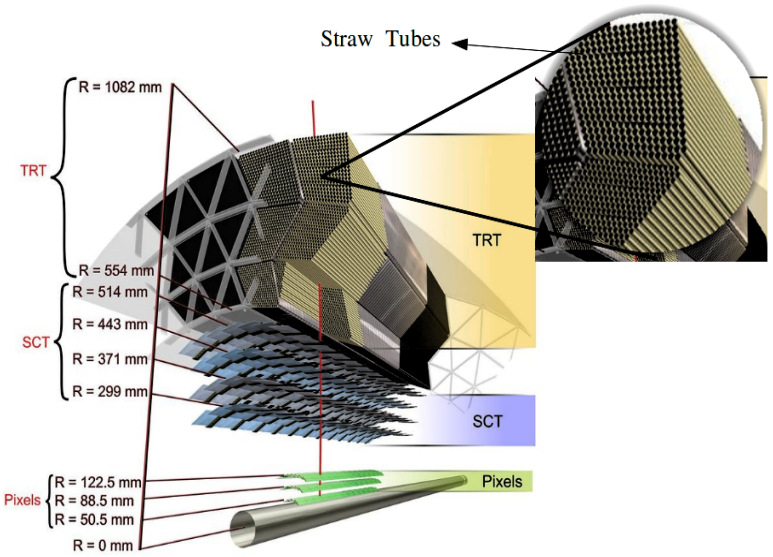

Figure 3.4: The inner detector sketch shows the three components plus the new insertable B-layer (IBL).

3.1.1 The Inner Detector

The inner detector (ID) is located at the center of the ATLAS detector near the interaction point and it has a diameter of 2.1 m. The ID is used for the measurements of the muon tracks close to the interaction point, providing accurate measurements of the track parameters inside the 2 Tesla magnetic field. It is also used to identify and track particles coming from the primary and secondary vertices. There are three main subsystems in the inner detector: the Pixel Detector, the Semiconductor Tracker (SCT) and the Transition Radiation Tracker (TRT). The diagram in figure 3.3 [38] shows the dimensions and sub-components of the inner detector. The pixel detector and the SCT are both made of silicon semi-conductors and together they constitute what is known as the silicon tracker, with pixel detector being the closest sub-component to the interaction point. The three sub-sections (Pixel detector, SCT and the TRT) and their radial distances from the beam pipe are shown in figure 3.4 [39]. In order to have better track and vertex reconstruction performance at the higher luminosities that were expected during Run 2 of the ATLAS detector and to mitigate the effect of radiation damage to the innermost layer of the pixel detector, a fourth layer, the insertable B-layer [40] was installed into the ATLAS inner detector system.

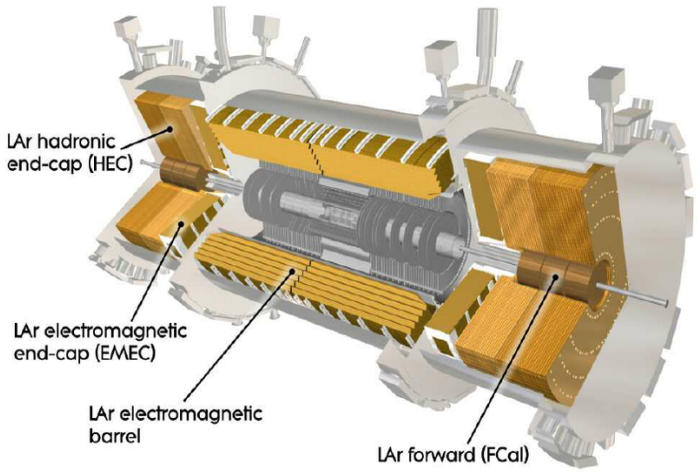

Figure 3.5: The sketch of the ATLAS LAr Calorimeter systems.

The silicon tracker provides space-point (R, ϕ and z) measurements for all particles that interact with it. Three space point measurements are registered in the pixel detector and four measurements are registered in the SCT on average. When charged particles cross the silicon sensors, they generate electron-hole pairs which are then used to track the position of the particle inside the detector. The Transition Radiation Tracker is the largest of the Inner Detector systems. It consists of approximately 300 000 drift tubes (straws) and each of the tubes is filled with a 70% Xe, 27% CO_2 and 3% O_2 gas mixture [41].

3.1.2 Calorimeters

The calorimeter system of the ATLAS detector surrounds the inner detector. The Calorimeter system measures the energy of photons, electrons and hadrons. It consists of the electromagnetic and hadronic Calorimeters. Each of these is a sampling calorimeter with an absorbing material inserted where the particle energy is deposited. Liquid Argon is an active detecting medium for the electromagnetic Barrel, Electromagnetic End-Cap, Hadronic End-Cap and the Forward Calorimeters.

3.1.2.1 Liquid Argon Calorimeters

The first part of the ATLAS Calorimeter system consists of the Liquid Argon (LAr) Calorimeters. These are the LAr Electromagnetic Barrel (EMB) Calorimeter, Electromagnetic End-Cap (EMEC) Calorimeter, Hadronic End-Cap (HEC) Calorimeter and the Forward Calorimeter (FCal). The Electromagnetic calorimeter

is divided into Barrel, End-Cap and Forward Calorimeters covering the pseudo-rapidity range $|\eta| \leq 1.475$, $1.375 \leq |\eta| \leq 3.2$ and $3.1 \leq |\eta| \leq 4.9$, respectively, and they all use Liquid Argon as an active material. It is used to measure the energy of electrons and photons that go past the inner detector. It is made with Liquid Argon as an active detecting material and Lead absorbers in the barrel and End-Cap sections. The energy of the incident particle is deduced from the measured energy loss of the particle shower. The design energy resolution for the Electromagnetic Calorimeter is given by:

$$\frac{\sigma(E)}{E} = \frac{a}{\sqrt{E(GeV)}} \oplus \frac{b}{E(GeV)} \oplus c, \tag{3.4}$$

where a is called the stochastic term, b is the electronic noise term and c is a constant term [42]. The hadronic calorimeter is another Liquid Argon Calorimeter located just after the Electromagnetic Calorimeter. Hadronic showers are formed when the incident hadron interacts with the detector material.

3.1.2.2 Tile Calorimeter

The Tile Calorimeter (TileCal) forms part of the hadronic Calorimeter and is installed just outside of the LAr Calorimeters. It is used to measure hadronic activity in the central region of the ATLAS detector up to a pseudo-rapidity of $|\eta| \leq 1.7$ [43]. Steel is used as an absorber and scintillating tiles are used as a detecting material. Ionizing particles cause the scintillator to emit ultraviolet light which is directed to photo-multiplier tubes (PMT). The PMT generates electrons which are collected at the cathode as an electrical signal. The energy resolution in the hadronic Calorimeter differs depending on the pseudo-rapidity region:

$$\frac{\sigma(E)}{E} = \frac{50\%}{\sqrt{E(GeV)}} \oplus 3\% \qquad for\ |\eta| \leq 3.2, \tag{3.5}$$

$$\frac{\sigma(E)}{E} = \frac{100\%}{\sqrt{E(GeV)}} \oplus 10\% \qquad for\ 3.2 \leq\ |\eta| \leq 4.9. \tag{3.6}$$

3.1.3 The Muon Spectrometer

The muon spectrometer (MS) is the outermost part and is also the largest part of the ATLAS detector, covering the pseudo-rapidity region $|\eta| \leq 2.7$. The Muon Spectrometer consists of one barrel ($|\eta| \leq 1.05$) and two endcaps ($1.05 \leq\ |\eta|\ \leq 2.7$). It consists of toroid magnets used to bend the muon tracks and muon chambers used for tracking and triggering. The toroid allows for the measurement of the momentum

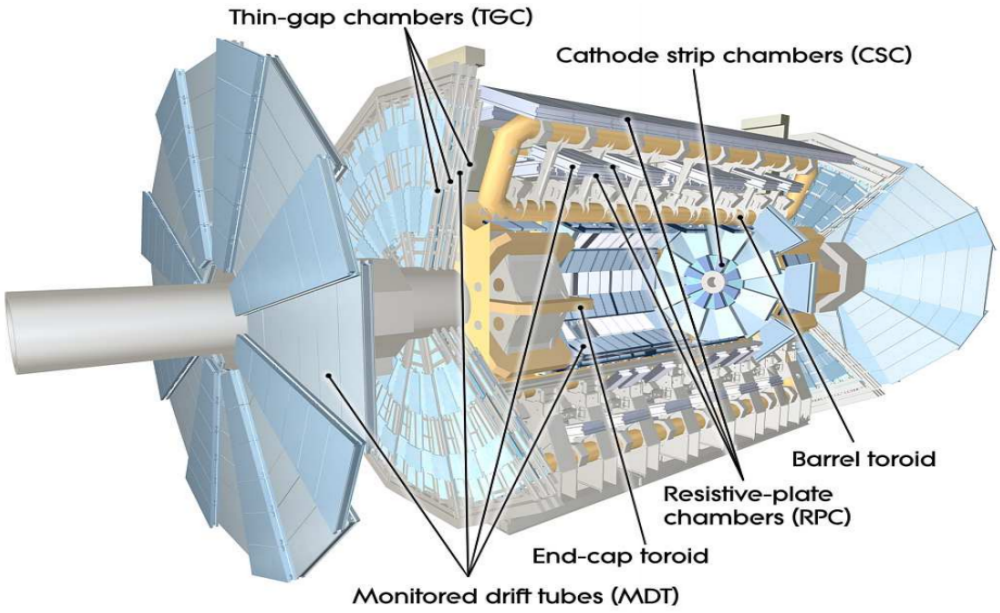

Figure 3.6: The schematic figure of the ATLAS muon spectrometer systems.

and trajectory of incident muon candidates. The muon spectrometer has four types of muon chambers installed: the Monitored Drift Tube (MDT), the Cathode Strip Chamber (CSC), the Resistive Plate Chamber (RPC) and the Thin Gap Chamber (TGC). The MDT and CSC are used for accurate measurements of the muon tracks in the central and forward regions. The MDT is made up of layers of tubes, each filled with a mixture of argon and carbon dioxide gasses. Resistive Plate Chamber (RPC) and Thin Gap Chamber (TGC) both constitute the trigger system in the barrel and end-cap regions, respectively. The RPC is devided into low-p_T and high-p_T trigger components. All the detector systems of the muon spectrometer are shown in figure 3.6 [44, 45].

3.1.4 The Trigger System

The trigger system helps to select only events with useful information for physics analysis. The ATLAS trigger system contains information from the different detector systems and allows for the removal of events that were recorded when the detector was not functioning as expected. The *pp*-collision rate at the peak luminosity reaches 40 MHz. The system is divided into three levels: level 1 trigger, level 2 trigger and the Event Filter. Level 2 and Event Filer together constitute what is known as the High Level Trigger (HLT).

- **Level 1:** This is a hardware-based trigger level. It selects objects such as electrons, photons, jets and high-p_T muons. Muon candidates are identified

using the RPC and TGC muon chambers. All events passing level 1 trigger are transferred to trigger level 2.

- **Level 2:** This is the second level in the ATLAS trigger system and unlike level 1, level 2 is software-based. Events from the level 1 Region of Interest are subjected to further selection requirements and those that satisfy the requirements in this level are transferred to the final level. This has the output rate of 2kHz.

- **Event Filter:** The event filter is the final level of the ATLAS trigger system. Events that pass at least one of the algorithms in level 2 are allowed for processing with the average processing time of 4 seconds per event.

In Run 2, Level 2 and Event Filter are merged and referred to as the High Level Trigger. The net output rate of the HLT is 1kHz. Only events that pass all trigger levels are stored for the analysis.

Chapter 4

Object Reconstruction and Event Selection

The description of the analysis channel is given in this section. Data as well as signal and background Monte Carlo samples used in the analysis are introduced. Heavy scalar searches are conducted in many Higgs boson decay modes at the LHC. These include a number of final states such as di-photon ($h \to \gamma\gamma$) decay channel as well as different multi-lepton final states. In this section, emphasis is placed more on the secondary decay of the heavy Higgs particle to a multi-lepton final state. The $H \to ZZ \to 4l$ channel features an excellent electron and muon mass resolution and a high signal to background ratio inside the signal region. For high mass studies, the heavy Higgs boson decays to two on-shell Z-bosons, each decaying to a pair of same flavor opposite sign (SFOS) leptons. This results in one quadruplet with four isolated leptons in the final state. Compared with other Higgs boson decay modes, the $H \to ZZ \to 4l$ channel has small background events in the signal region due to its easy-to-reconstruct final state objects. The most dominant background is the non-resonant $qq \to ZZ$ and $gg \to ZZ$ productions, which have the same four lepton signature. This makes the ZZ background difficult to suppress. Other small background contributions to the $H \to ZZ \to 4l$ signal region are from $t\bar{t}$ and Z+jets contributions. The $t\bar{t}$ and Z+jets backgrounds are reduced by applying impact parameter requirements and isolation requirements to all events that enter the signal region.

4.1 Data and MC Samples

4.1.1 Data Samples

Data from pp collisions are subjected to strict quality requirements and only data from the ATLAS good run list (GRL) is used. This is the data that pass

all quality checks or data recorded when the detector is functioning according to expected standards. All data that fail the quality requirements are marked for removal and will not be used in the analysis. The data was recorded at the center of mass energy of $\sqrt{s} = 13$ TeV and corresponds to the integrated luminosity of 36.2 fb^{-1} for 2015+2016 data, 43.6 fb^{-1} for 2017 data, 59.9 fb^{-1} for 2018 data and 140 fb^{-1} for all 2015 to 2018 data combined.

4.1.2 Signal MC Samples

Vector boson fusion and gluon-gluon fusion signal samples are used for the analysis. All signal samples were generated with Powheg Box v2 [46] Monte Carlo generator. Powheg calculates ggF and VBF at next-to-leading order (NLO) in QCD. The Powheg generator is interfaced to Pythia 8 [47] for parton showering and hadronization and using NNPDF23LO [48, 49] PDF set for the hard scattering process. Signal samples used have mass points between $m_H = 200$ GeV and $m_H = 1000$ GeV at 100 GeV intervals from the narrow-width approximation (NWA).

4.1.3 Background MC Samples

Background in the $H \to ZZ \to \ell^+\ell^-\ell^+\ell^-$ decay channel consist of contributions from $qq \to ZZ$, $gg \to ZZ$, $t\bar{t}$ and Z+jets events that enter the signal region. The $qq \to ZZ$ background contribution is simulated with Sherpa v2.2.1 [50] generator with NNPDF3.0NNLO PDF set [51] for the hard scattering process. The $gg \to ZZ$ and tri-boson (ZZZ and WWW) contributions are simulated with Sherpa v2.1.1 event generator at leading order (LO) in QCD. Powheg Box v2 is used to model the $t\bar{t}$ events with Pythia 6 used for parton showering and hadronization.

4.1.4 Main Background

The four lepton channel is dominated by the non-resonant ZZ production from gluon-initiated and quark-initiated processes. This is the main background affecting the HZZ studies because it also leads to the four lepton final state like the signal process. The $qq \to ZZ$ background account for approximately 86% of the total background in the $H \to ZZ \to 4\ell$ channel, 10% for the $gg \to ZZ$ and 4% for all other contributions ($t\bar{t}$ and Z+jets) combined. The Z-boson does not couple directly with the gluons so it is necessary to go through the heavy-fermion loop, as shown in figure 4.1 (b).

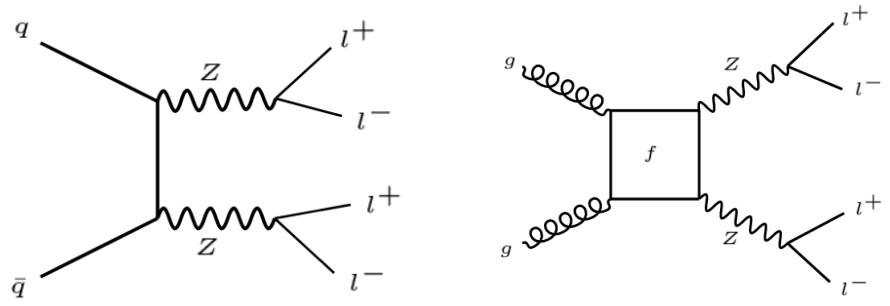

(a) (b)

Figure 4.1: Feynman diagrams for the non-resonant ZZ production of four-lepton events through the (a) quark- and (b) gluon-initiated processes.

The number of $qq \to ZZ$ and $gg \to ZZ$ background events is estimated using Monte Carlo simulation.

4.1.5 Additional Background

The reducible background component to the $H \to ZZ \to 4\ell$ channel comprises Z+jets and $t\bar{t}$ events, as well as another small contribution to the reducible background coming from WZ events. Reducible background results from light flavor jets that are misidentified as electrons and muons.

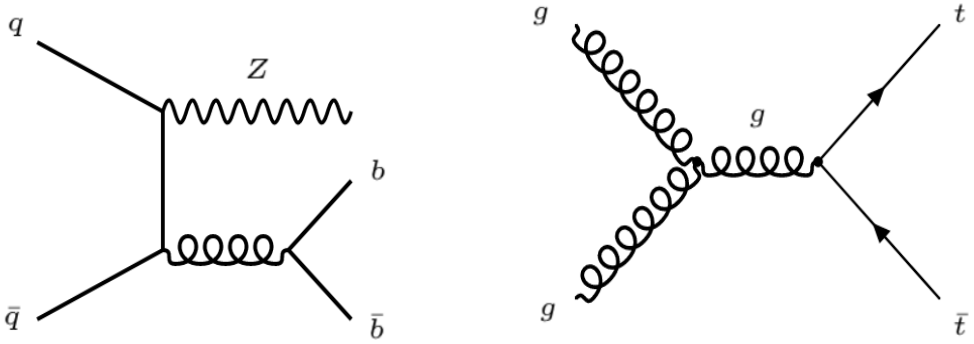

(a) (b)

Figure 4.2: Feynman diagrams for the reducible background processes showing (a) Z+jets and (b) $t\bar{t}$ production at the LHC energy scale.

It is estimated using both Monte Carlo simulation and data-driven methods. This background component is suppressed by imposing impact parameter and isolation requirements on all events that enter the signal region. The Reducible back-

ground composition depends on the flavor of leptons that make the sub-leading pair in the quadruplet. This background is therefore usually separated into $\ell\ell + e^+e^-$ and $\ell\ell + \mu^+\mu^-$ categories. The $\ell\ell + \mu^+\mu^-$ category includes events from Z+jets and $t\bar{t}$ backgrounds shown in figure 4.2. The Z+jets background is a contribution from both heavy-flavor ($b\bar{b}$) and light-flavor jets. To estimate the number of events (yield) for the $\ell\ell + \mu^+\mu^-$ category, four control regions (CR) are defined. These are inverted impact parameter significance control region, inverted isolation CR, same sign CR on the sub-leading pair and different flavor CR on the leading pair. Each of these control regions is designed to improve the statistics of one or more of the background processes. The number of events obtained in the control region are extrapolated to the signal region using transfer factors. The $\ell\ell + e^+e^-$ category arises from light-flavor jets that are misidentified as prompt electrons, from photon conversion as well as the leptonic decays of heavy-flavour hadrons. The $3\ell + X$ control region with three leptons selected with nominal selection criteria and one lepton (X) with relaxed selection criteria is defined using data-driven techniques. Extrapolating to the signal region requires the use of transfer factors which are calculated using Monte Carlo simulation.

4.2 Signal Production

The production of the Higgs-like candidates at the LHC proceeds via four main production mechanisms. The most dominant production mechanism according to the production cross-section is the gluon-gluon fusion mechanism. This is followed by the vector boson fusion production as discussed in section 2.4.2. Other important production mechanisms of the Higgs boson at the LHC consist of the associated production with the vector boson (ZH or WH) as well as the associated production with a pair of top quarks (ttH). Out of the four main production modes, the ggF production mechanism contributes about 88% to the total Higgs-like production cross-section. Contributing about 7% to the total cross-section, the vector boson fusion mechanism is the second most dominant process at the LHC. 4% and 1% contributions to the total cross-section come from the higgstrahlung (VH) and ttH processes, respectively.

4.3 Object Reconstruction

Each particle leaves a unique signature in a specific part of the ATLAS detector. To extract signal events from different background contributions in the signal region, it is necessary to define the expected final state objects and to define a selection

criteria for choosing clean signal events.

4.3.1 Electrons

Two detector systems are critical to reconstruct electron candidates in ATLAS. Clusters in the Electromagnetic calorimeter are identified and then matched with the particle tracks from the inner detector system. All electron candidates must be in the pseudo-rapidity range $|\eta| \leq 2.47$ and within a cone of $\Delta R = 0.2$. Positive and negative charge electrons are identified by the direction towards which their curved tracks go. Loose, medium or tight-likelihood working point is used to identify electron candidates. The suppression of heavy flavour background contribution is improved by adding the transverse impact parameter and transverse impact parameter significance to the likelihood discriminant.

4.3.2 Muons

Muon candidates are reconstructed by matching all tracks in the inner detector with information from the muon spectrometer. All muon candidates must be in the pseudo-rapidity range $|\eta| \leq 2.7$ and within a cone of $\Delta R = 0.3$. Depending on the reconstruction, four types of muon objects can be distinguished: stand alone muon, combined muon, segment-tagged muon and calorimeter-tagged muon. For stand alone muon type, the particle track (trajectory) is reconstructed using only information from the muon spectrometer. Combined muon consist of tracks in the inner detector and tracks in the muon spectrometer which are then combined with a global fit. Segment-tagged muon consists of segments in the Monitored Drift Tube and Cathode Strip Tube muon chambers which are matched with tracks in the inner detector. Segment-tagged muon objects increase the acceptance for low-p_T muons. Tracks associated with energy deposits in the ATLAS calorimeter give rise to calorimeter-tagged muon candidates.

4.3.3 Jets

The anti-k_T-algorithm[1] with a distance parameter $R = 0.4$ is used to reconstruct jets [52]. Jets from pile-up events are suppressed by imposing a requirement on the the jet vertex fraction which ensures that only jets from the primary vertex are considered. Jet reconstruction algorithms help to distinguish between events from VBF, ggF and VH production modes. Jet objects are requested within the pseudo-rapidity range $|\eta| \leq 4.4$ and a transverse momentum requirement of $p_T \geq 25$ GeV.

[1] Anti-k_T is a clustering algorithm that is used to select only calorimeter cells with significant energy deposits. More information on the anti-k_T-algorithm can be found in Reference [52].

4.4 Four-lepton Event Selection

For high mass analysis in the $H \to ZZ \to 4\ell$ decay channel, events with exactly four leptons (one quadruplet) are selected in four different channels or categories ($4e, 4\mu, 2\mu 2e$ and $2e2\mu$) with only muon and electron candidates as part of the final state. We select 2μ2e or 2e2μ by choosing a pair closest to the mass of the Z-boson (91.2 GeV) [53] so instead of using four channels we tend to combine 2μ2e and 2e2μ into one channel and call it 2μ2e. All four lepton events are required to originate from a vertex with at least two associated tracks [54]. To reconstruct the final state objects for the four lepton channel, electrons are required to have $p_T \geq 7$ GeV and with $|\eta| \leq 2.47$. Requirements for muon candidates is $p_T \geq 5$ GeV and with $|\eta| \leq 2.7$. Not more than one calorimeter-tagged, segment-tagged or stand-alone muon candidate in the pseudo-rapidity range $2.5 \leq |\eta| \leq 2.7$ is allowed per quadruplet.

4.4.1 Quadruplet Selection

The Higgs boson candidate is obtained by selecting one quadruplet (two same flavour opposite sign lepton pairs) with $p_T \geq 20, 15, 10$ GeV for the first three leading leptons. The separation requirement of $\Delta R = \sqrt{(\Delta\eta)^2 + (\Delta\phi)^2} \geq 0.10$ (0.20) for same- (different-) flavour leptons are required and all quadruplets containing a pair of leptons with invariant mass smaller than 5 GeV are vetoed. This requirement on the di-lepton invariant mass helps to reduce the contamination from J/ψ mesons in the analysis. The leading lepton pair is chosen by selecting a pair with invariant mass (m_{12}) closest to the mass of the Z-boson and is required to be between 50 GeV and 106 GeV. The invariant mass of the third and fourth leptons in the quadruplet (m_{34}) is required to be in the range ($m_{th} \leq m_{34} \leq 115$ GeV) where m_{th} is the threshold mass and ranges between 12 GeV and 50 GeV, depending on the invariant mass of the quadruplet and it remains 50 GeV for high mass studies ($m_{4l} \geq 190$ GeV). The threshold (m_{th}) increases linearly with m_{4l} from the lower value of 12 GeV to the highest value of 50 GeV in the range 140 GeV $\leq m_{4l}$.

4.4.2 Isolation and Impact Parameter

Calorimeter-based and track-based isolation variables are used to separate isolated electron candidates (prompt electrons) from the final state objects originating from hadronic decays and mis-identified as electrons. The track-isolation discriminant, defined as the sum of the transverse momenta of tracks inside a cone of size ΔR = 0.3 (0.2) around the muon (electron) excluding the lepton track itself, divided

by the p_T of the lepton, is required to be smaller than 0.15. The calorimeter-based isolation discriminant similarly adds up the cluster E_T values used to reconstruct jets within a cone of width $\Delta R = 0.2$ around the barycentre of the candidate lepton. The E_T sum divided by the p_T of the lepton needs to be smaller than 0.3 for muon objects and 0.2 for electron objects.

The longitudinal impact parameter requirement of less than 10 mm for both electrons and muons is required, while the transverse impact parameter requirement of 1 mm is applied for muons. This requirement allows for identification of events that are not from the primary vertex (background events). The primary vertex is defined as the vertex with the largest $\sum p_T^2$ which is calculated from associated tracks, while the others are identified as pile-up vertices. The requirement on the transverse impact parameter significance $|d_0/\sigma d_0| \leq 3.5$ for muons and $|d_0/\sigma d_0| \leq 6.5$ for electrons must also be fulfilled [55], where d_0 represents the distance of closest approach to the interaction point and σd_0 is the error associated with d_0. Track-based isolation requirements, calorimeter-based isolation requirements, primary vertex constraint as well as the impact parameter requirements on lepton candidates help with the suppression of the sub-dominant $t\bar{t}$ and Z+jets background contributions [56]. The requirement for tracks to originate from the primary vertex is used to suppress contribution from pile-up [57] events.

4.4.3 Overlap Removal

To prevent over-counting of the reconstructed events, all overlapping events are removed by requiring all events to be separated from other objects with clusters and/or tracks. Overlaps between leptons is prevented by requiring that $\Delta R(\ell, \ell) \geq 0.1$ between leptons of the same flavour and $\Delta R(\ell, \ell) \geq 0.2$ between leptons of different flavours. The overlap between electrons and jets is prevented by removing any jet candidate that appear within $\Delta R(e, jet) \leq 0.2$. The overlap between muons and jets is removed by removing any jet candidate that appear within $\Delta R(\mu, jet) \leq 0.1$.

4.5 Pile-up

The Instantaneous luminosity for ATLAS increases from 2015 to 2018 data-taking period. With an increase in the total luminosity comes an increase in the average number if interactions per proton bunch crossing (pile-up). The change in the luminosity from 2015 to 2018 and the average number of interactions per bunch

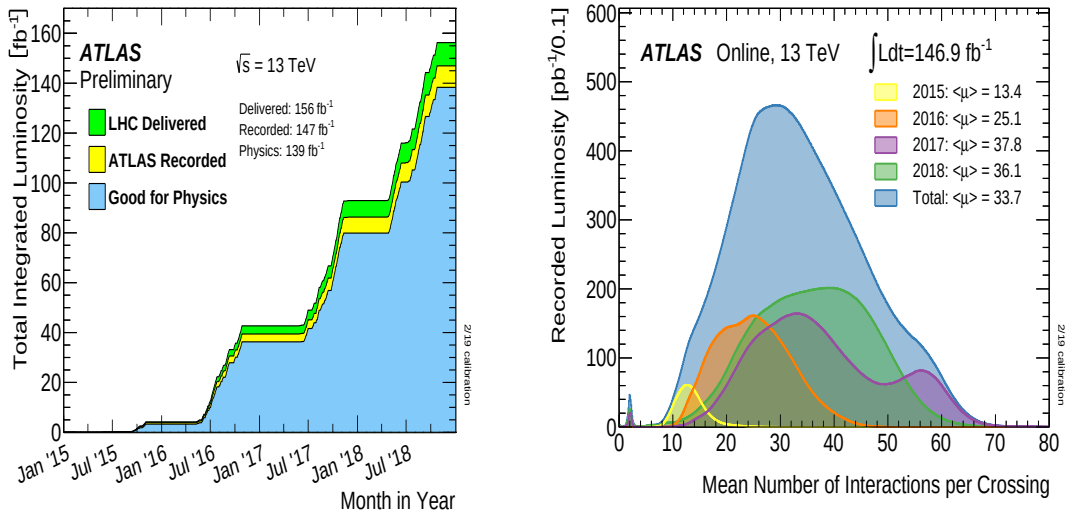

(a) (b)

Figure 4.3: The luminosity for the 2015 to 2018 data-taking period in figure (a), and the mean number of interactions per proton bunch crossing in figure (b).

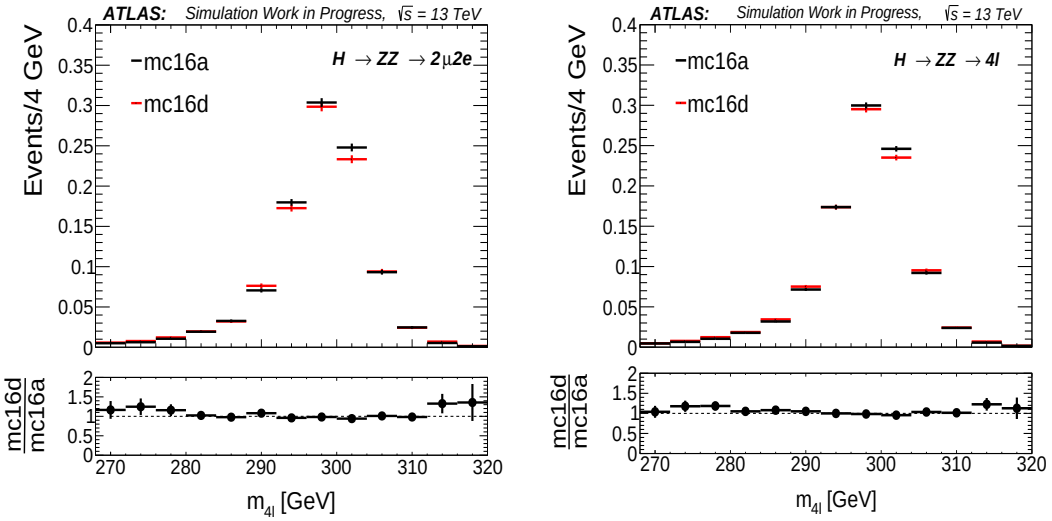

(a) (b)

Figure 4.4: Comparison of mc16a with mc16d using the m_{4l} distribution for the (a) $2\mu 2e$ and (b) 4ℓ final state.

crossing are shown in figure 4.3. The luminosity plot shows clearly the luminosity of the data delivered by the LHC, the luminosity of the data recorded by the ATLAS detector as well as the luminosity for the data that is good for use in performing physics analysis (data from the ATLAS good-run-list). Pile-up results from additional proton-proton collisions occurring at the same time as the collision of interest.

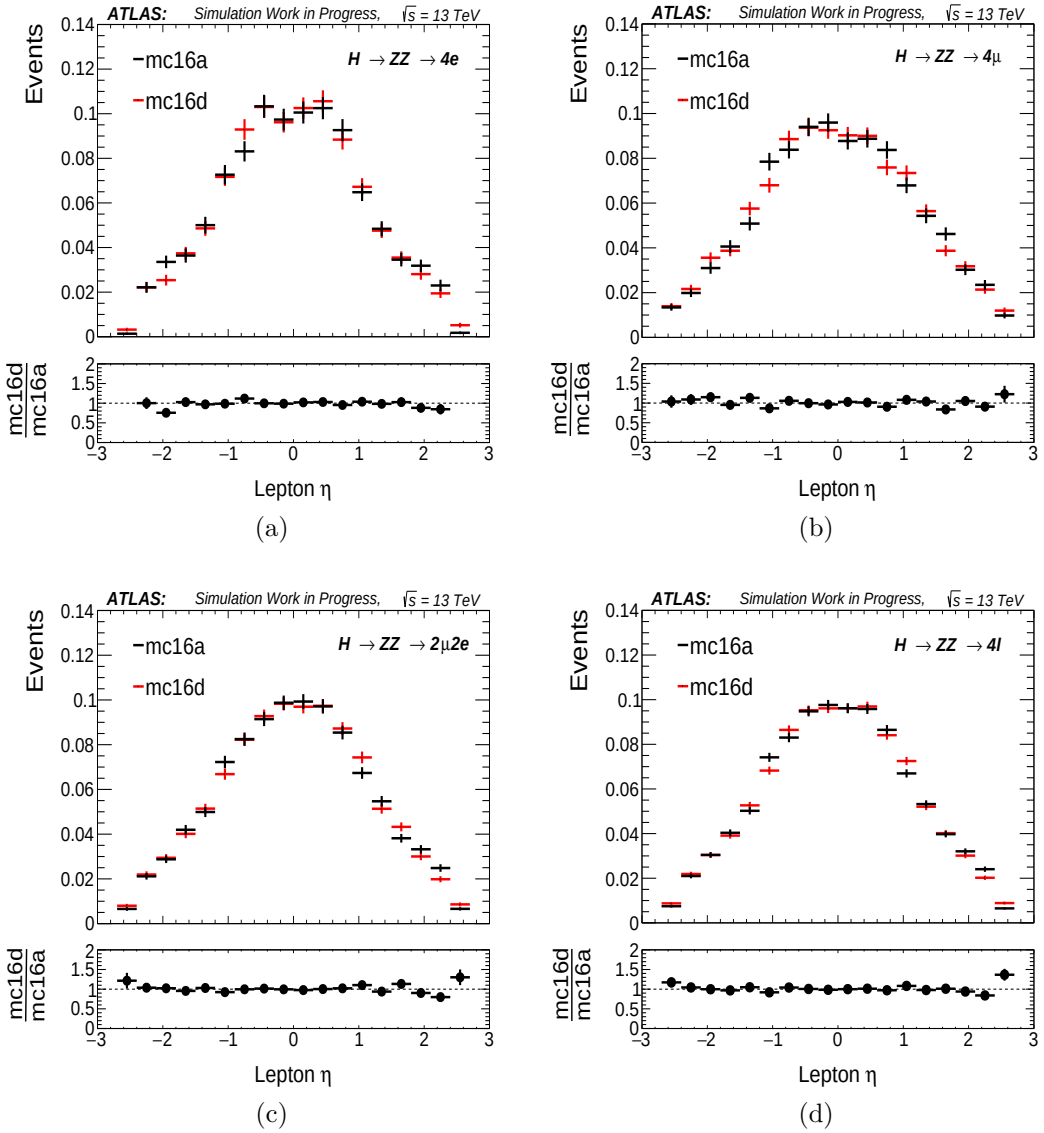

Figure 4.5: Comparison of the shapes of mc16a with mc16d using the η distribution for the positive charge lepton of the leading Z-boson in the (a) $4e$, (b) 4μ, $2\mu 2e$ and (d) 4ℓ final state.

Two types of pile-up events can be distinguished: the in-time pile-up and out-of-time pile-up. The earlier results from multiple interactions within the same proton bunch occurring at approximately the same time, and the later results from interactions in different nearby proton bunches occurring at approximately the same time. This difference in pile-up is expected between the Monte Carlo corresponding to the data recorded during the 2015+2016 data-taking period (mc16a) and the Monte Carlo corresponding to the data recorded during the 2017 data-taking period (mc16d). This change in pile-up may affect the shapes of the signal and background kinematic distributions and the number of events between mc16a and

mc16d. One may be able to see if there is any effect that this change in the pile-up conditions has by comparing shapes of the kinematic variables and the number of background events. Any significant deviation in the shape of these distributions may be an indication of the effect of pile-up between mc16a and mc16d samples. These comparisons are shown in figure 4.4 and 4.5. The number of expected $qq \to ZZ$ background events for mc16a and mc16d was also compared. Since we are comparing samples with different integrated luminosity, we normalize both of them to the same luminosity to ensure fair and correct comparison of the number of events. Table 4.1 shows the expected irreducible background ($qq \to ZZ$) yield which is calculated in the range 140 GeV $\leq m_{4\ell} \leq$ 800 GeV.

Table 4.1: $qq \to ZZ$ background yields in the mass range 140 GeV $\leq m_{4\ell} \leq$ 800 GeV.

	$\mathbf{4}\ell$	$\mathbf{4}\mu$	$\mathbf{4}e$	$\mathbf{2}\mu\mathbf{2}e$
MC16a	806.05	249.92	157.76	398.38
MC16d	776.49	240.28	152.44	383.78
$\frac{MC16a}{MC16d}$	1.038	1.040	1.035	1.038
% difference	3.8	4.0	3.5	3.8

The study shows no significant deviation in the shapes of the signal distributions due to the change in the pile-up conditions and only 3.8 percent difference in the number of background events between mc16a and mc16d samples in the inclusive (4ℓ) final state is observed as shown in table 4.1.

4.6 High Mass Parameterization

4.6.1 The Signal Model

The high mass signal for the Narrow-Width resonance is modelled using the sum of a Gaussian function and a Crystal Ball function. Narrow-width signal samples with mass points from 200 GeV to 3000 GeV for both ggF and VBF production mechanisms are used. The probability density function (PDF) used for narrow-width signal modelling is defined by:

$$P_s(m_{4l}) = f_C \times C(m_{4l}; \mu, \sigma_C, \alpha_C, n_C) + (1 - f_C) \times G(m_{4l}; \mu, \sigma_G). \tag{4.1}$$

The width of the crystal ball function (σ_C) is different from that of a Gaussian function (σ_G), while the mean (μ) is the same for both functions and the parameter (fC) is used to control the relative normalizations of the Gaussian and Crystal Ball. The α_C and n_C parameters are used to control the tail of the crystal ball

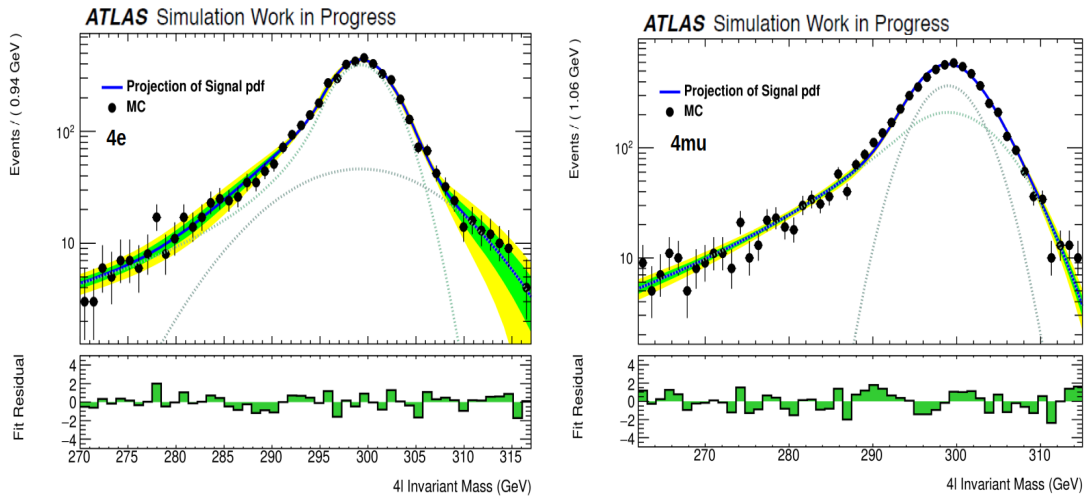

(a) (b)

Figure 4.6: Example of the fitted $m_{4\ell}$ distribution in the (a) $4e$ final state and (b) 4μ final state for $m_H = 300$ GeV mass point.

function. The signal parameterization is done separately for ggF production mode and VBF production mode. All mass point from 200 GeV to 3 TeV are used for signal parameterization, but only the distributions for $m_H = 300$ GeV in the $4e$ and 4μ final states are shown in figure 4.6. The green dotted line represents the Crystal Ball function and the gray dotted line is the Gaussian function. The tail of the signal distribution in the final state with electrons ($4e$ and $2\mu 2e$) is described by both Gaussian and Crystal Ball functions but in the 4μ channel, the tail is described by the Crystal Ball function only.

4.6.2 The Background Model

The m_{4l} distribution for $qq \to ZZ$ and $gg \to ZZ$ background is parameterized by an empirical function and with Monte Carlo simulation. The function used for the background model can be written as:

$$f_{ZZ}(m_{4l}) = (f_1(m_{4l}) + f_2(m_{4l})) \times H(m_0 - m_{4l}) \times C_0 + f_3(m_{4l}) \times H(m_{4l} - m_0). \quad (4.2)$$

The off-shell analysis in the low mass region is described by the first part (f_1) and f_3 describes the tail in the high mass part of the $m_{4\ell}$ spectrum. The normalization factor C_0 ensures that the function is continuous around m_0 and is defined as

$$C_0 = \frac{f_3(m_0)}{f_1(m_0) + f_2(m_0)}. \quad (4.3)$$

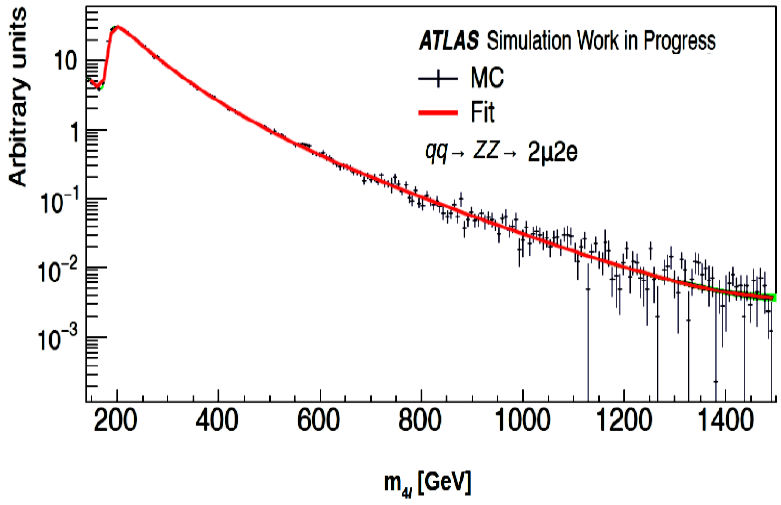

Figure 4.7: A fit to the $qq \to ZZ$ background in the $2\mu 2e$ channel.

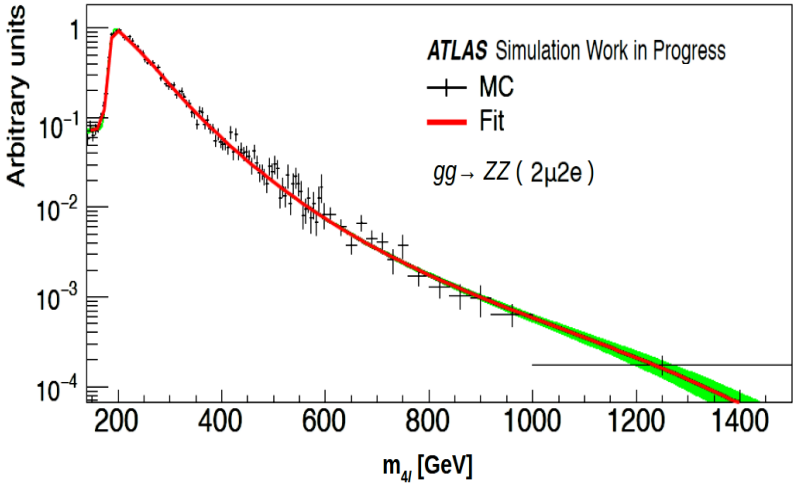

Figure 4.8: A fit to the $gg \to ZZ$ background in the $2\mu 2e$ channel.

The other parts of the function can be written as:

$$f_1(m_{4\ell}) = e^{(a_1 + a_2 m_{4\ell} + a_3 m_{4\ell}^2)}, \tag{4.4}$$

$$f_2(m_{4\ell}) = \left[\frac{1}{2} + \frac{erf(m_{4\ell} - b_1)}{2b_2}\right] \times \frac{1}{1 + e^{\left(\frac{m_{4\ell} - b_1}{b_3}\right)}}, \tag{4.5}$$

$$f_3^{qqZZEW}(m_{4\ell}) = Exp(c_1 + c_2 m_{4\ell} + c_3 m_{4\ell}^2 + c_4 m_{4\ell}^{2.7}), \tag{4.6}$$

$$f_3^{qqZZ,ggZZ}(m_{4\ell}) = Exp(c_1 + c_2 m_{4\ell} + c_3 m_{4\ell}^2 + c_4 m_{4\ell}^3 + c_5 m_{4\ell}^4 + c_6 m_{4\ell}^5). \tag{4.7}$$

The letters a_i, b_i and c_i represent the shape parameters obtained by fitting the invariant mass distribution for all categories using the ZZ background Monte Carlo.

A fit to the $qq \to ZZ$ distribution is shown in figure 4.7 and a fit to the $gg \to ZZ$ distribution is shown in figure 4.8 using the $m_{4\ell}$ distribution in the $2\mu 2e$ final state.

4.7 High Mass Acceptance

Signal acceptance is defined as a ratio of the number of events passing the selection for $H \to ZZ \to 4\ell$ channel (introduced in section 4.4) to the total number of generated events in each final state for ggF and VBF production modes.

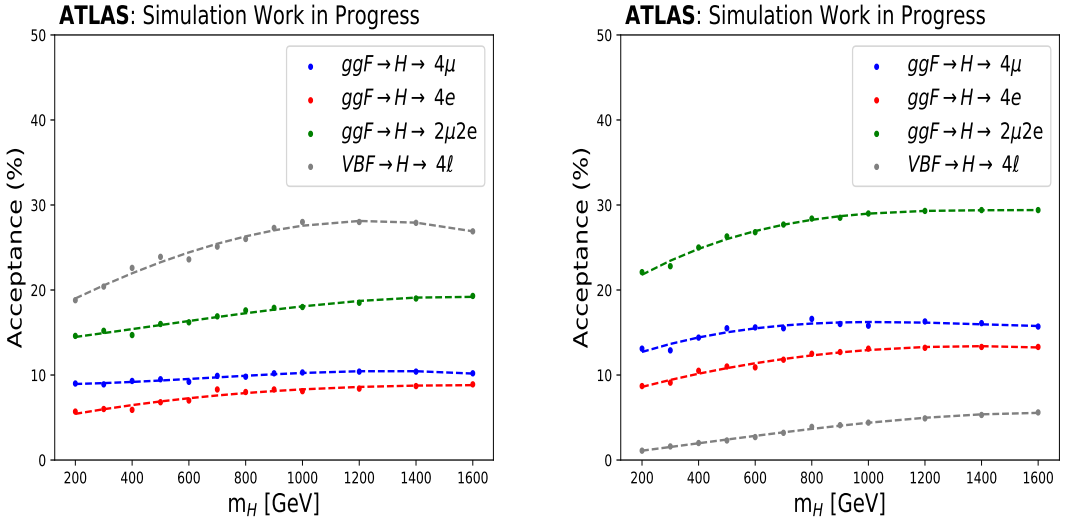

(a) (b)

Figure 4.9: High mass Signal Acceptance for each production mode with cut-based categorization. The plots show three ggF categories as well as one VBF category for (a) VBF production and (b) ggF production.

The contribution from tau lepton decays is not included in the calculation of acceptance. These calculations were done for cut-based VBF categorization where events with two or more jets and satisfying $m_{jj} \geq 400$ GeV and $\Delta\eta_{jj} \geq 3.3$ are selected for the VBF category and merging all Monte Carlo campaigns (mc16a, mc16d and mc16e). For high mass studies, both Z-bosons are on-shell so it is only the measurement resolution that decides which way the pairing occurs. We select $2\mu 2e$ or $2e2\mu$ by choosing a pair with the invariant mass closest to the mass of the Z-boson (91.2 GeV) so instead of using four channels, we combine $2\mu 2e$ and $2e2\mu$ into one channel called $2\mu 2e$. Signal samples from 200 GeV to 1600 GeV are used and the acceptance is calculated separately for ggF and VBF production modes.

Table 4.2: Signal acceptance for ggF and VBF production modes in the four-lepton channel calculated using all Monte Carlo campaigns. The Acceptance is shown for m_H = 200 GeV to m_H = 500 GeV resonance mass points.

m_H	Prod-mode	ggF-category			VBF-category
		4μ	$4e$	$2\mu 2e$	4ℓ
200 GeV	ggF	13.1%	8.7%	22.1%	1.1%
	VBF	9.0%	5.7%	14.6%	18.8%
300 GeV	ggF	12.9%	9.1%	22.8%	1.6%
	VBF	8.9%	6.0%	15.2%	20.4%
400 GeV	ggF	14.4%	10.5%	25.0%	2.0%
	VBF	9.3%	5.9%	14.7%	22.6%
500 GeV	ggF	15.5%	11.0%	26.3%	2.3%
	VBF	9.5%	6.8%	16.0%	23.9%

Table 4.3: Signal acceptance for ggF and VBF production modes in the four-lepton channel calculated using all Monte Carlo campaigns. The Acceptance is shown for m_H = 600 GeV to m_H = 900 GeV resonance mass points.

m_H	Prod-mode	ggF-category			VBF-category
		4μ	$4e$	$2\mu 2e$	4ℓ
600 GeV	ggF	15.6%	10.9%	26.8%	2.7%
	VBF	9.2%	7.0%	16.0%	23.6%
700 GeV	ggF	15.5%	11.8%	27.7%	3.2%
	VBF	9.9%	8.3%	16.9%	25.1%
800 GeV	ggF	16.6%	12.5%	28.4%	3. 9%
	VBF	9.8%	8.0%	17.6%	26.0%
900 GeV	ggF	16.0%	12.7%	28.5%	4.1%
	VBF	10.2%	8.3%	17.9%	27.5%

4.8 High Mass Control Region

Comparison of 2018 data sample with the corresponding Monte Carlo sample (mc16e) in the Side band is performed. The number of events and some distributions in this region are presented in this section. The study was conducted to check for discrepancies between 2017 data and 2018 data events, as well as 2018 data and Monte Carlo (mc16e) events. A cut is applied on the four lepton invariant mass requiring only events satisfying 70 GeV $\leq m_H \leq$ 110 GeV and 140 GeV $\leq m_H \leq$ 200 GeV mass range in order to select the Control Region for high mass analysis. As it is evident in the table and in figure 4.10, the presented yields are calculated in the side band without contribution from the gluon induced irreducible background ($gg \rightarrow ZZ$) events. The observed discrepancy between data and MC in the side band is expected in this case given that the $gg \rightarrow ZZ$ contribution ($\approx 10\%$ of the total background) to the Monte Carlo was not included in the calculation of the number of events shown in figure 4.10 and in table 4.4.

Table 4.4: The number of events for the 2018 data and mc16e samples in the side band [70 GeV, 110 GeV] and [140 GeV, 200 GeV] with 59.9 fb^{-1}.

Channel	$qq \rightarrow ZZ$	Z**+jets**, $t\bar{t}$	**Data 2018**	**Data/MC**
4μ	166.2	1.149	205	1.225
4e	87.5	1.444	95	1.069
2μ**2e**	189.1	3.182	241	1.253
4ℓ	442.8	5.776	541	1.206

The lepton transverse momentum for the positive charge lepton in the leading lepton pair and the rapidity of the four-lepton system is shown in figure 4.10. The leading lepton pair is defined as a pair with the invariant mass closest to the mass of a Z boson (see section 4.4.1). A similar study was also done by comparing 2017 data with 2018 data using the same selection of events. The distributions in figure 4.11 show the comparison between 2017 and 2018 data sets. To ensure a fair comparison of the two samples, 2017 data was re-scaled to the total luminosity of the 2018 data sample (59.9 fb^{-1}). The study shows good agreement in the number of events between 2017 and 2018 data in the high mass side band.

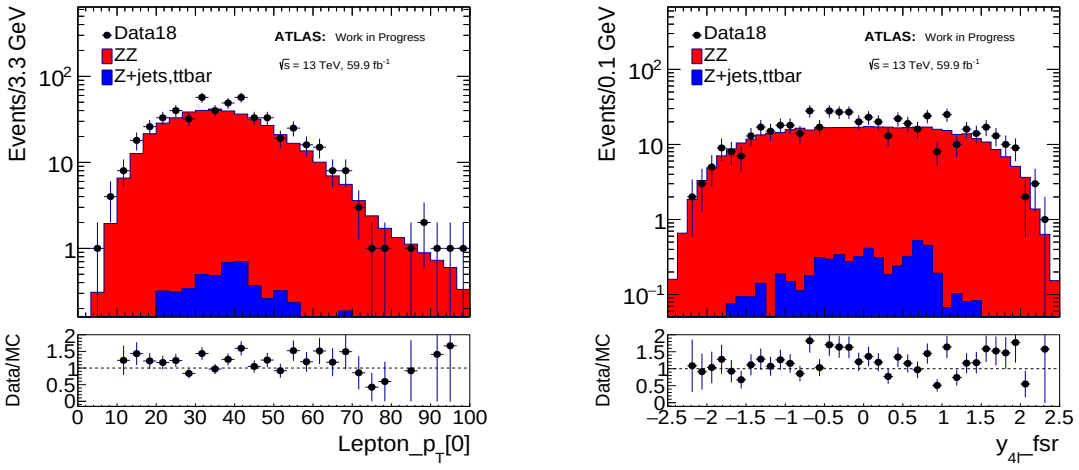

(a) (b)

Figure 4.10: Comparison of the 2018 data set with mc16e using (a) The transverse momentum of a positive charge lepton in the leading lepton pair and (b) the rapidity of the four-lepton system.

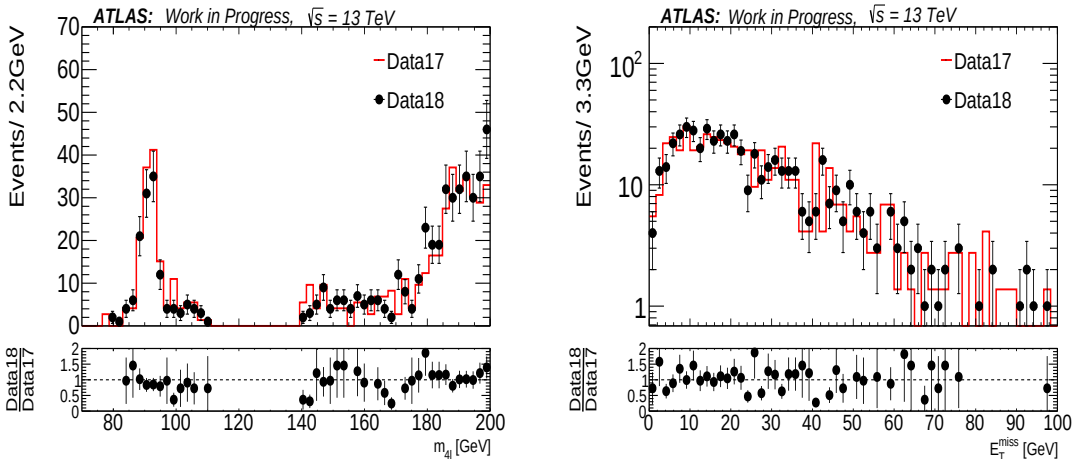

(a) (b)

Figure 4.11: Comparison of 2017 data set with the 2018 data set using (a) four lepton invariant mass and (b) the missing transverse energy.

Chapter 5

Event Categorization for Narrow Resonance Searches

The categorization of events into ggF and VBF categories is discussed in this chapter for the $H \to ZZ \to 4\ell$ analysis channel. This can be done in at least three different ways: the cut-based VBF classifier, Deep Neural Network (DNN) [58, 59] classifier and a Boosted Decision Tree (BDT) [60, 61] classifier. A cut-based categorization method is used in this chapter with only a brief summary of the DNN categorization method also introduced in section B.2. This study aims to provide selection cuts that can be used to distinguish signal events produced via vector boson fusion production mode from events that are produced via the gluon fusion production mode. Events are classified as VBF or ggF categories using the optimized selection as will be discussed in section 5.1. Events passing the optimized selection cuts are classified into the VBF-enriched category and all remaining events are classified into ggF-enriched category. This provides a method to obtain selection cuts at which the sensitivity of the VBF production mode is maximum.

The characteristic two jet signature of the VBF production mode is explored during the selection of the VBF events and is used for choosing clean signal events as shown in section 5.1. The procedure shown here applies to the high mass searches in the $H \to ZZ \to 4\ell$ channel and assumes the production of a narrow-width resonance (NWA). The distributions of the features that were used in the cut-based classifier are shown in figure 5.1 for the $m_H = 300$ GeV signal mass point.

5.1 Cut-based Categorization

The optimization study based on the signal (VBF) selection efficiency and background (ggF) rejection is presented in this section. The ϵ(S)$\times$[1- ϵ(B)] 2D maps are

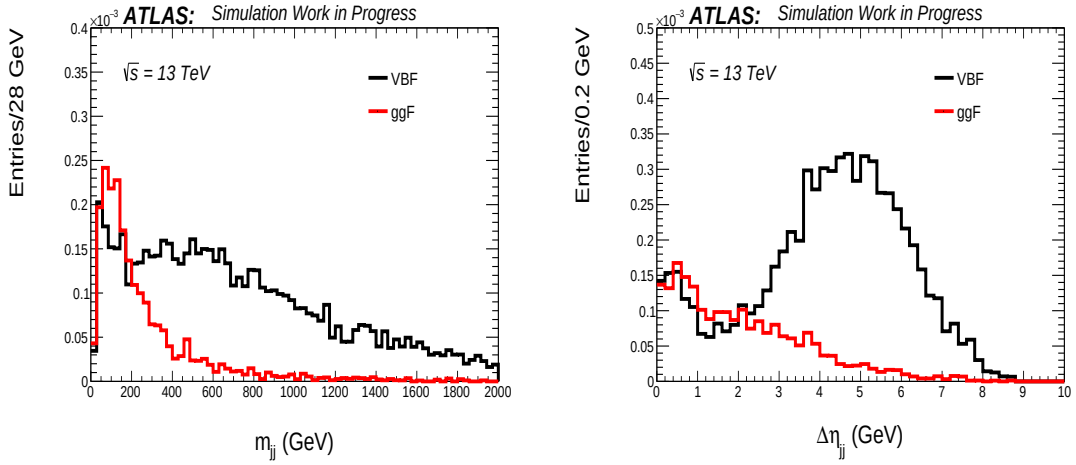

(a) (b)

Figure 5.1: Two important features used for the selection of VBF signal events. The invariant mass of the two leading jets and $\Delta\eta_{jj}$ defined as $\eta_{j1} - \eta_{j2}$ are shown in (a) and (b) respectively for the $m_H = 300$ GeV mass point.

used to choose the most optimal selection cuts (m_{jj} and $\Delta\eta_{jj}$) for each signal mass point. The variable ϵ(S) represents the signal selection efficiency , ϵ(B) represents the background efficiency and 1- ϵ(B) is the background rejection. The purpose of this study was to see if better cuts on m_{jj} and $\Delta\eta_{jj}$ can be found if the full Run 2 Monte Carlo with the total integrated luminosity of 140 fb^{-1} is used for optimization of the VBF signal. All VBF and ggF mass points between 200 GeV and 1000 GeV are used in the study. Signal samples in this mass range are simulated in steps of 100 GeV as mentioned in section 4.1.2.

This section presents the VBF selection efficiency, ggF rejection as well as maps showing the product of VBF selection efficiency and ggF rejection. By combining ϵ(S)$\times$[1- ϵ(B)] maps from all sample mass points and using this to determine the m_{jj} and $\Delta\eta_{jj}$ cuts corresponding to the maximum value, the overall optimal cut-based selection that can be used for all signal mass points considered in this study can be obtained. The obtained m_{jj} and $\Delta\eta_{jj}$ cuts can then be compared with the current standard cuts ($m_{jj} \geq 400$ GeV and $\Delta\eta_{jj} \geq 3.3$) to check if there is any improvement in the VBF signal efficiency and background rejection with respect to the currently used cuts. The decision on the final optimal cut-based selection depends mainly on its ability to maintain high signal selection efficiency and high background rejection across all signal mass points that were used in the study.

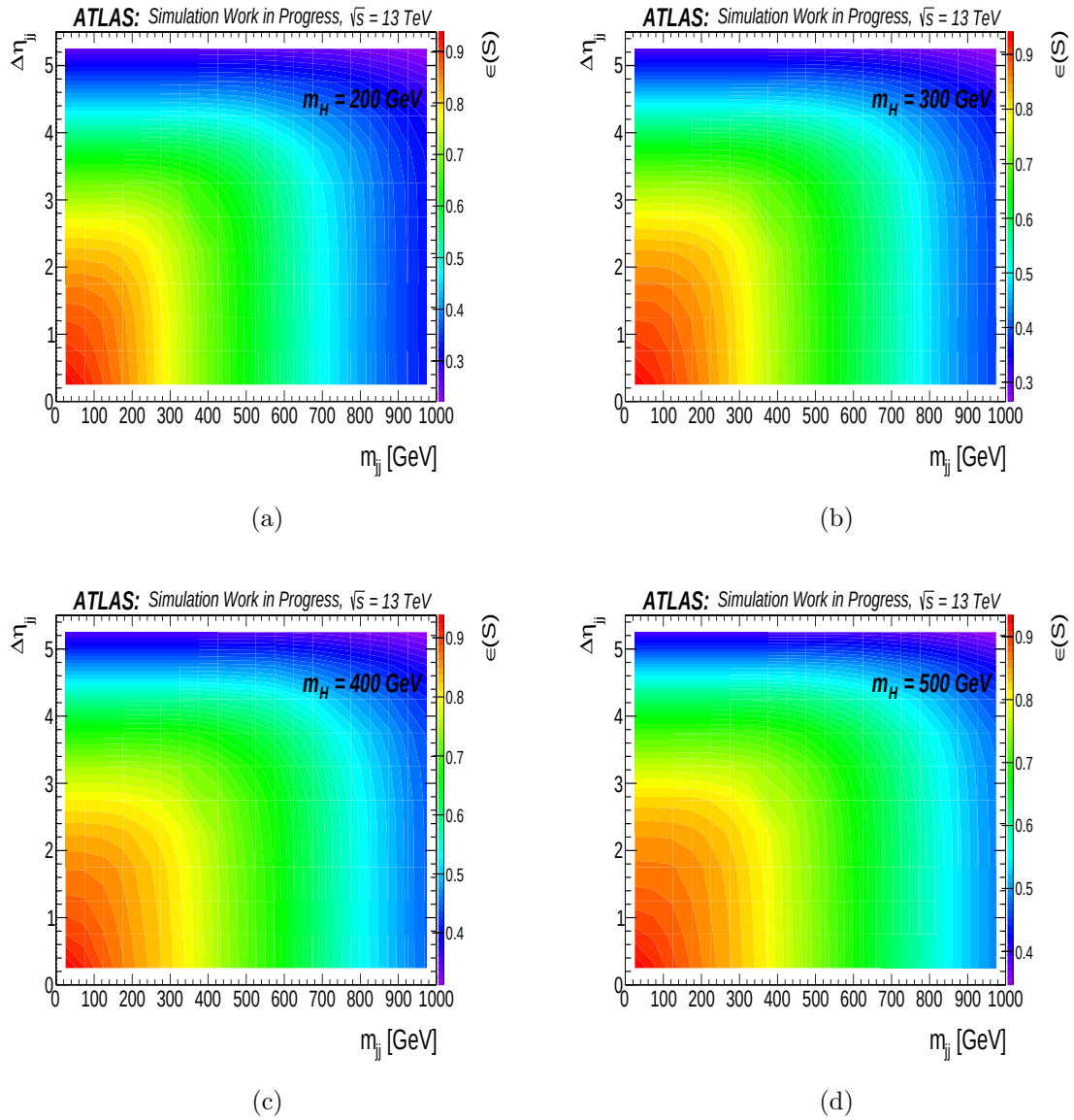

(a) (b)

(c) (d)

Figure 5.2: Signal selection efficiency maps for (a) m_H = 200 GeV, (b) m_H = 300 GeV, (c) m_H = 400 GeV and (d) m_H = 500 GeV mass points.

5.1.1 Selection Efficiency

The signal selection efficiency was calculated as the ratio of the number of events after the VBF selection cuts to the number of events before the VBF selection cuts was applied. Four efficiency maps are displayed in figure 5.2 for the m_H = 200 GeV, m_H = 300 GeV, m_H = 400 GeV and m_H = 500 GeV signal mass points. The rest of the figures can be found in section B.1.

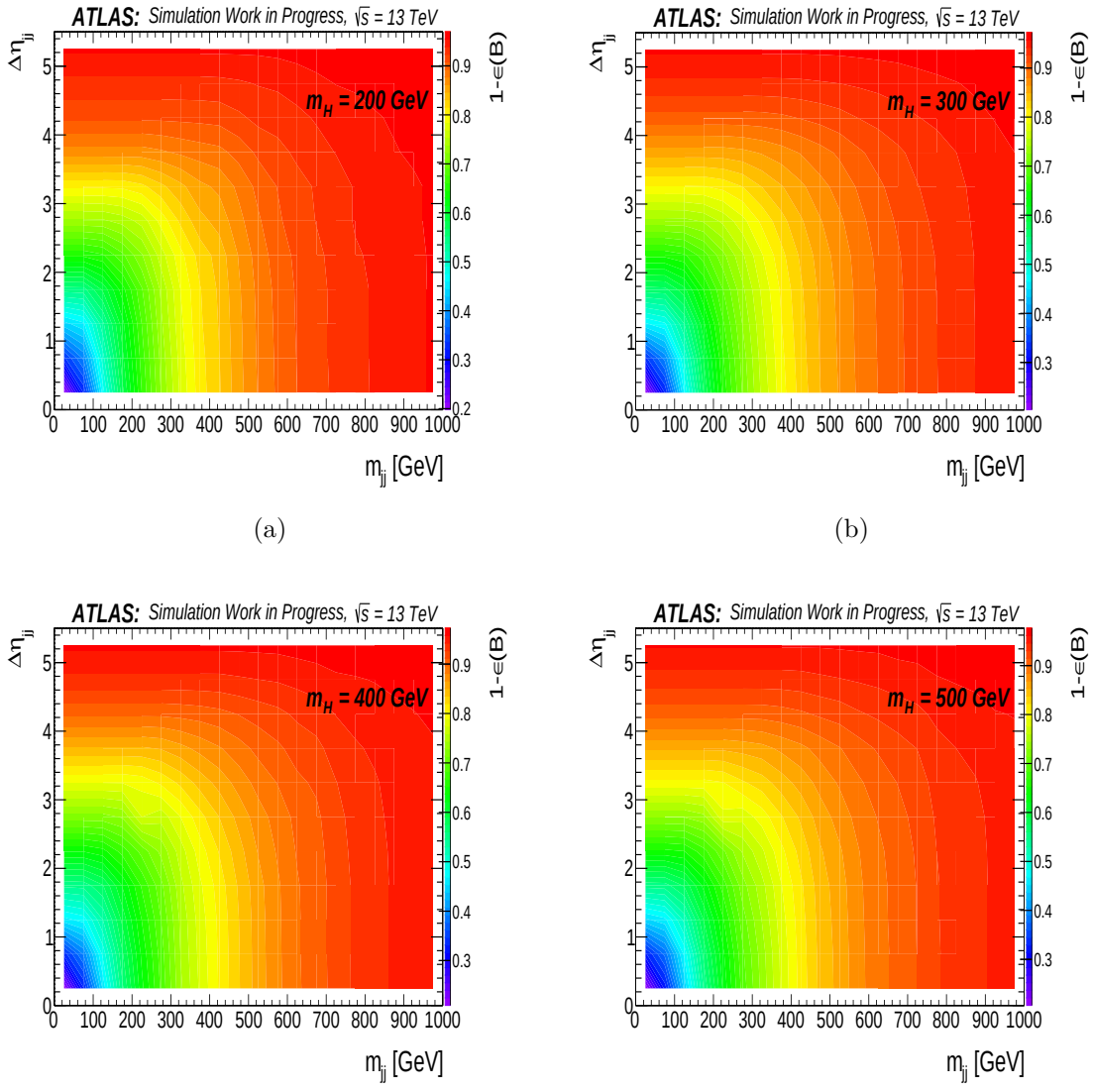

(a) (b)

(c) (d)

Figure 5.3: background rejection maps only for the (a) m_H = 200 GeV, (b) m_H = 300 GeV, (c) m_H = 400 GeV and (d) m_H = 500 GeV mass points.

5.1.2 Background Rejection (1-ϵ(B))

To define background rejection in the VBF signal region, a fraction of non-VBF events that are removed during the selection is calculated and it is the measure of the ability of each applied selection cut to reject ggF events in the VBF signal region. Background rejection is calculated in the 200 GeV to 1000 GeV mass range. The maps for m_H = 200 GeV, m_H = 300 GeV, m_H = 400 GeV and m_H = 500 GeV mass points are displayed in figure 5.3 and the rest of the maps in section B.1.

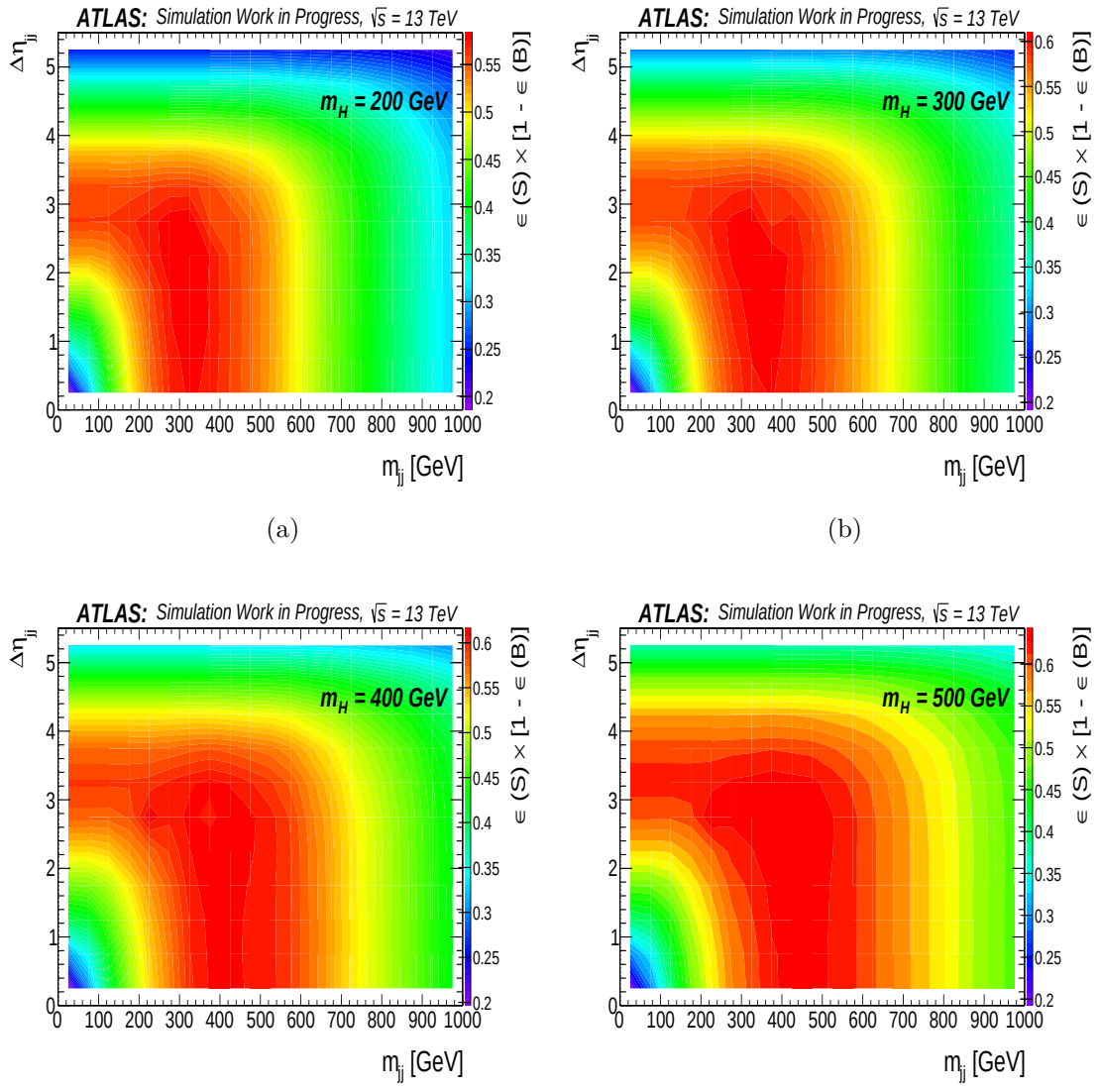

(a) (b)

(c) (d)

Figure 5.4: ϵ(S) $\times$ [1- ϵ(B)] maps for the (a) m_H = 200 GeV, (b) m_H = 300 GeV, (c) m_H = 400 GeV and (d) m_H = 500 GeV mass points.

5.1.3 Product (ϵ(S) $\times$ [1- ϵ(B)])

The ϵ(S) $\times$ [1- ϵ(B)] plot is used to choose optimal selection cuts for each sample in the 200 GeV $\leq m_H \leq$ 1000 GeV mass range. The plots in figure 5.4 were obtained by multiplying the selection efficiency with the background rejection. To find the selection that can be used for all mass points, the sum of all ϵ(S) $\times$ [1- ϵ(B)] maps can be used as shown in figure 5.5.

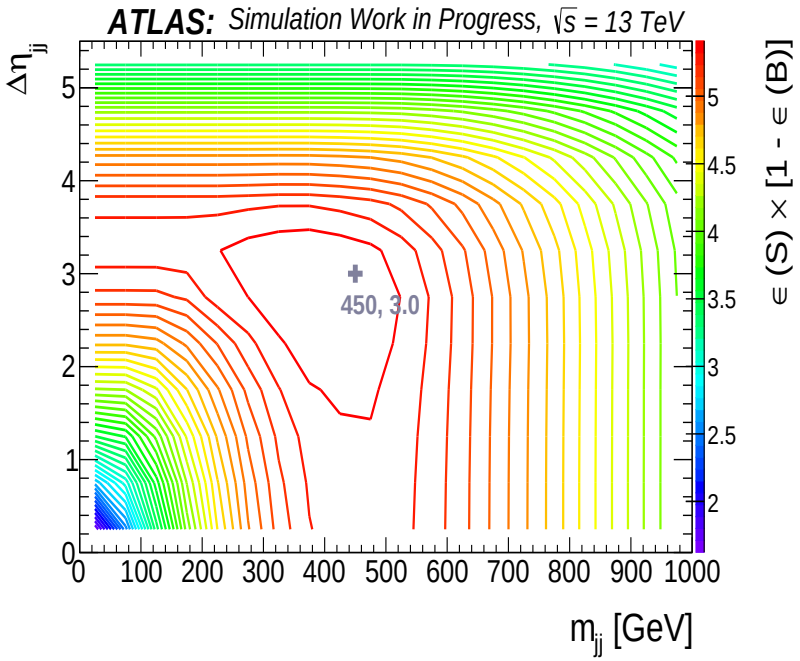

Figure 5.5: The ϵ(S)×[1-ϵ(B)] 2D map for all nine mass points (m_H = 200 GeV to m_H = 1000 GeV) and it provides the most optimal selection for all nine samples that were used for event categorization.

Combinations of m_{jj} (0 GeV to 1000 GeV) and $\Delta\eta_{jj}$ (0 to 5.5) cuts are investigated in figure 5.4 and the optimal selection for each mass point is chosen by finding the cuts corresponding to the maximum value of ϵ(S)×[1-ϵ(B)]. This method provides selection cuts with good ability to reject non-VBF events and still maintain high signal selection efficiency. Signal efficiency and background rejection are important features required when choosing the optimal selection cuts. Choosing a very tight cut may result in excellent background rejection but very low signal efficiency. The opposite is also true, choosing a loose cut may result in high signal selection efficiency but poor background rejection. This trade-off can be seen clearly in figure 5.6 as a small increase in background rejection and a small decrease in the signal efficiency for the new cuts. The maximum value of the product ϵ (S)×[1-ϵ(B)] obtained in figure 5.5 reveals the new optimal selection cuts for all nine mass points that were used. The currently used standard VBF selection requires events with two or more jets with p_T greater than 30 GeV, are well separated in η and satisfying $m_{jj} \geq 400$ GeV and $\Delta\eta_{jj} \geq 3.3$. Comparison of the new selection that is obtained in this section with the standard VBF selection is discussed in section 5.2.

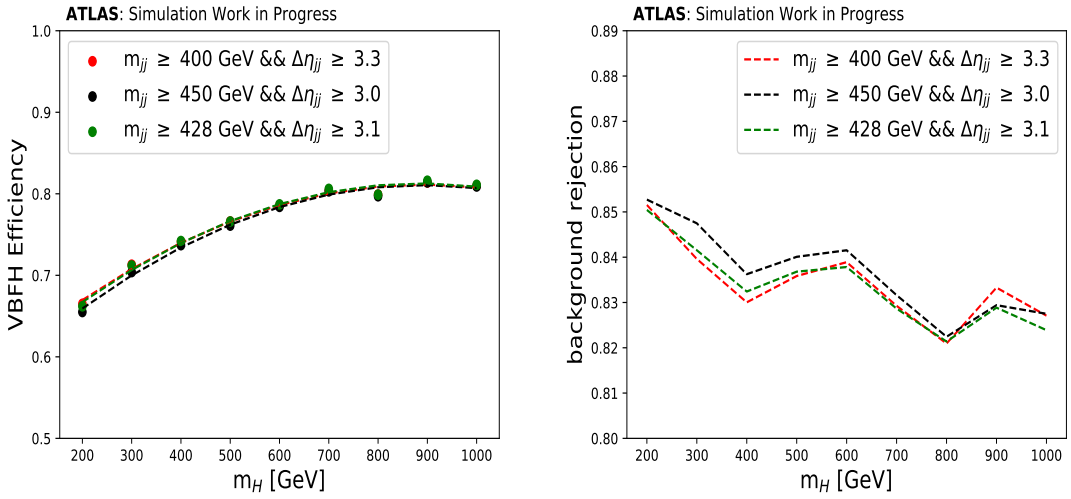

(a) (b)

Figure 5.6: Selection efficiency (a) and background rejection (b) as a function of mass of the resonance for the optimal selection in the VBF category.

5.2 Summary of Results

The final optimal selection is decided by comparing cuts obtained in figure 5.5 (the new selection) with the currently used selection in the VBF category. In figure 5.6 (a) and figure 5.6 (b), a third set of cuts ($m_{jj} \geq 428$ GeV and $\Delta\eta_{jj} \geq 3.1$) is included and this was obtained by taking the average of the cut values over all mass points that are used in this study. The two sets of selection cuts obtained here are compared with the standard cuts that are currently used for VBF selection. This comparison is done to look for improvements in the selection efficiency and background rejection for the chosen optimal selection with respect to the standard cuts. These comparisons are shown in figure 5.6. The black line is the new selection shown in figure 5.5, the green line is a new selection cut obtained by taking the average over all mass points and the red line shows the currently used standard cut which is used here as a reference cut-based selection. It can be seen in figure 5.6 (a) and figure 5.6 (b) that the current selection is still good enough to use as cut-based VBF selection with high signal selection efficiency across all mass points. The new cuts appear to have similar effect on the events in comparison with the standard selection with only small differences in selection efficiency and background rejection over the mass range considered in this study. It is recommended to keep the current standard cuts ($m_{jj} \geq 400$ GeV and $\Delta\eta_{jj} \geq 3.3$) as optimal selection method for cut-based event categorization in the $H \to ZZ \to 4\ell$ channel. All events passing this

selection are classified into the VBF category and the selection can be used to search specifically for narrow resonances produced via the VBF production mode. The rest of the events are classified into any one of the three ggF categories depending on the lepton flavour composition of the final state (4μ, $4e$ and $2\mu 2e$).

Chapter 6

Conclusions

The work presented in this research is related to the searches for heavy resonances in the $H \rightarrow ZZ \rightarrow 4\ell$ channel. The production of a heavy resonance with Higgs-like decay modes via the vector boson fusion mechanism was the primary focus. In order to search separately for resonances produced via the vector boson fusion production mechanism, it is necessary to define a clear criteria for selecting only VBF signal events. To achieve this, a cut-based VBF categorization study was conducted using signal selection efficiency and background rejection. The method presented here provides a way to separate events produced via the VBF production mode from events that are produced via the ggF production mode. Events that pass the optimized selection are classified in the VBF-enriched category and the rest of the events are classified in any one of the three ggF-enriched categories according to the flavour of leptons in the final state. Optimization of the VBF selection was performed using selection efficiency and background rejection 2D maps and using ggFH and VBFH samples in the 200 GeV $\leq m_H \leq$ 1 TeV mass range. The study was done using Monte Carlo samples only and by choosing events with two or more jets with p_T greater than 30 GeV and requiring that all events passing the optimized selection cuts be categorized into VBF-enriched category. It was found that the currently used selection is still good enough for use in the cut-based categorization of VBF and ggF events with full Run 2 Monte Carlo corresponding to the total integrated luminosity of 140 fb^{-1}. It is recommended therefore to keep the current cuts ($m_{jj} \geq$ 400 GeV and $\Delta\eta_{jj} \geq 3.3$) as optimal cut-based selection to use for narrow resonance searches.

The categorization of events in this study was done using the standard cut-based method and it aimed only to distinguish VBF events from the ggF events in the $H \rightarrow ZZ \rightarrow 4\ell$ analysis channel. The results presented here are valid only for resonant searches in the $H \rightarrow ZZ \rightarrow 4\ell$ high mass ($m_H \geq$ 200 GeV) analysis.

Current studies are also focusing on the categorization using a deep neural network classifier (see reference [2]) in order to try and improve from the optimized cut-based selection. The DNN-based categorization features a dedicated VBF classifier called VBF-DNN and a dedicated ggF classifier called ggF-DNN. As in the cut-based categorization, the DNN-based categorization study is also valid for high mass studies in the $H \to ZZ \to 4\ell$ channel where the production of a narrow-width resonance is assumed. A brief summary of the DNN-based event categorization is given in section B.2. The final cut-based and DNN-based selection results can be summarized as follows:

Cut-based categorization

- VBF-4ℓ: All events with two or more jets and $\mathrm{m}_{jj} \geq 400$ GeV and $\Delta\eta_{jj} \geq 3.3$.
- ggF-(4μ, $4e$ and $2\mu 2e$): All remaining events enter into this category.

DNN-based categorization

- VBF-4ℓ: All events with two or more jets AND VBF-DNN output score $>$ 0.8.
- ggF-(4μ, $4e$ and $2\mu 2e$): All events with less than two jets AND ggF-DNN output score > 0.5 OR events with two or more jets AND VBF-DNN output score < 0.8.
- Background: All remaining events.

The optimal selection cuts presented here were chosen based on good overall performance, high signal selection efficiency and with high background rejection across all mass points that are used in the optimization study. This cut-based selection can be used to select the VBF signal events in the 200 GeV $\leq m_H \leq$ 1000 GeV mass range and only for the narrow-width signal.

Appendix A

$A \to ZH$ Signal Optimization Study

The production of a heavy resonance in association with a Z-boson in $A \to ZH$ decays is discussed in this section. A heavy Higgs-like scalar which was first introduced in section 2.5 is produced here through the decay of a pseudo-scalar (A). This is done using fiducial mini-trees produced with the ATLAS $H4l$ Analysis Framework [62]. A heavy resonance is produced in association with a Z-boson as primary decay products of a CP-odd scalar with varied mass from $m_A = 350$ GeV to $m_A = 450$ GeV while the mass of the heavy scalar is fixed at $m_H = 250$ GeV for all masses of A. A heavy scalar is allowed to decay to four leptons through a pair of Z bosons ($H \to ZZ \to 4\ell$) and the associated Z-boson is allowed to decay to two neutrinos ($Z \to \nu\nu$), leading to the final state with one quadruplet (two same flavour opposite sign lepton pairs) plus missing transverse energy. The optimization study presented in this chapter is based only on one mass of the pseudo-scalar (m_A = 375 GeV) and is done only with Monte Carlo samples.

A.1 The Signal

Four lepton events are selected as described in the nominal selection for the $H \to ZZ$ analysis with a b-veto, two central jets and low missing transverse energy significance. A cut on E_T^{miss} or E_T^{miss} significance is decided by the optimization study, which is based entirely on Truth Monte Carlo (MC events without detector simulation). The E_T^{miss} suppression was not necessary due to low background in the four lepton channel signal region. All events are counted in the $m_{4l} \geq 130$ GeV and $m_{4l} \leq 400$ GeV mass window. Truth events for the signal ($A \to ZH(250),\ Z \to \nu\nu,\ H \to ZZ \to 4l$) were used to optimize the selection. The optimization study was performed using the $A(375)$ truth signal sample, as seen in section A.3.

A.2 Data and MC

Figure A.1 shows the data and Monte Carlo comparisons using the transverse momentum of the four lepton system (p_T^{4l}) and the number of jets distributions. The purpose of figure A.1 is to see if there is good agreement between data and Monte Carlo, which is also important to ensure that all background MC events are used in the study for the purpose of calculating the significance. This comparison is based on mc16a Monte Carlo and 2015+2016 data set, both corresponding to the integrated luminosity of 36.2 fb^{-1}.

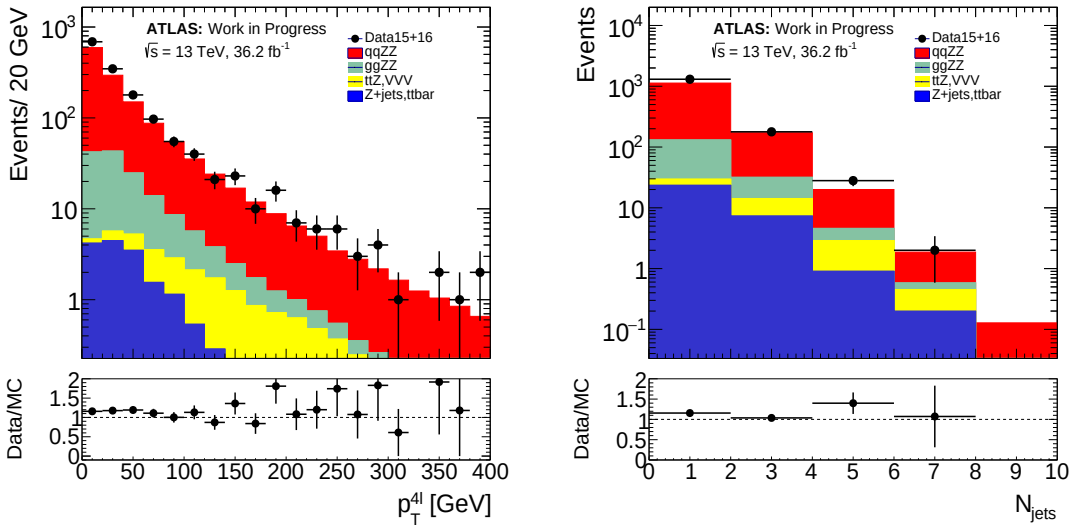

Figure A.1: Data and MC comparison using the distributions for the transverse momentum of the four leptons system p_T^{4l} (left) and the number of jets (right).

A.3 Optimizing the E_T^{miss} Cut

The signal is selected by choosing events with two or more central jets. Another cut requiring events with zero b-jets is applied in order to suppress the ttZ background contribution in the signal region. In addition to selecting events with two central jets and zero b-jets, a cut on the E_T^{miss} or E_T^{miss} significance also needs to be applied. The optimal cut on the missing transverse energy is obtained by finding a cut value with the maximum significance as shown in table A.1.

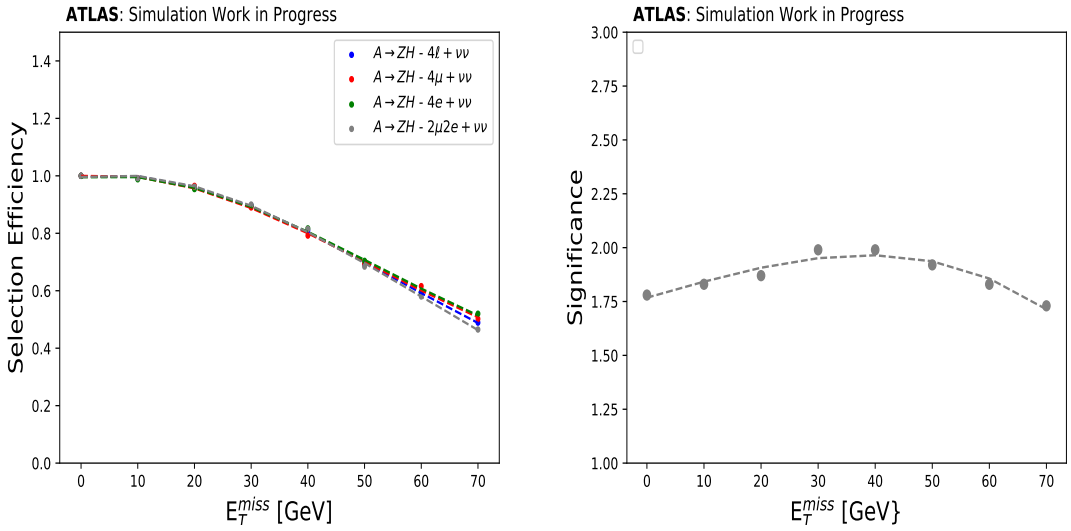

(a) (b)

Figure A.2: Selection efficiency for the $A \to ZH$ signal per final state (a) and the expected significance as a function of the E_T^{miss} cut (b).

Table A.1: The number of Signal and background MC events and the expected significance for each value of the E_T^{miss} cut.

$\mathbf{E_T^{miss}}$ >	$qq \to ZZ$	$gg \to ZZ$	ttZ	Z+**jets**	**Expected**	B	A**375**	$\frac{S}{\sqrt{S+B}}$
0	57.7	7.9	1.8	1.1	68.5	7.8	6.82	1.78
10	51.4	7.1	1.7	1.1	61.3	6.9	6.77	1.83
20	38.0	5.4	1.7	0.8	45.9	5.2	6.38	1.87
30	24.2	3.6	1.6	0.7	30.1	3.3	6.11	1.99
40	14.4	2.1	1.5	0.6	18.6	2.1	5.50	1.99
50	7.9	1.2	1.4	0.6	11.1	1.3	4.73	1.92
60	4.2	0.6	1.2	0.5	6.5	0.8	4.02	1.83
70	2.2	0.3	1.1	0.5	4.1	0.4	3.36	1.73

The number of events remaining after each E_T^{miss} cut from $E_T^{miss} \geq 0$ GeV to $E_T^{miss} \geq 70$ GeV is used in the definition of selection efficiencies shown in figure A.2 (a). The selection efficiency is calculated using the $A(375) \to ZH$ signal sample in the 4ℓ, 4μ, $4e$ and $2\mu 2e$ final states. The number of signal events and the expected background events is shown in table A.1. The main background consists of the non-resonant quark initiated ZZ ($\approx 86\%$), the gluon initiated ZZ ($\approx 10\%$) and the electroweak ZZ production which contributes approximately 1% to the total

background in this channel and becomes more significant in the VBF category. The cut value that represents the maximum significance is taken to be the most optimal cut for the $A \to ZH \to 4\ell\nu\nu$ signal events. The significance is estimated using:

$$Z = S/\sqrt{S+B}, \tag{A.1}$$

where S is the number of signal events and B is taken to represent the expected number of background events in the signal region (chosen to be within $\pm 3\sigma$ away from the mean of the $m_{4\ell}$ distribution). The estimated significance corresponds to each E_T^{miss} cut value as indicated in table A.1. The graph of the significance as a function of missing transverse energy has a maximum where the E_T^{miss} cut is greater than 30 GeV as shown in figure A.2 (b).

Appendix B

Event Categorization

As it was discussed in chapter 5, the signal event categorization for high mass analysis in the $H \to ZZ \to 4\ell$ channel is performed in this dissertation using a cut-based method. This was done to check if the currently optimized selection is still good enough to use during Run 2 analysis. This chapter shows the rest of the optimization figures that are not shown in chapter 5.

B.1 Cut-based Classifier

Selection efficiency for the signal events is shown in figure B.1 and figure B.2 for the 600 GeV, 700 GeV, 800 GeV and 900 GeV mass points. The signal selection efficiency shows the ratio of the number of events that pass each set of selection cuts to the total number of events before the VBF selection.

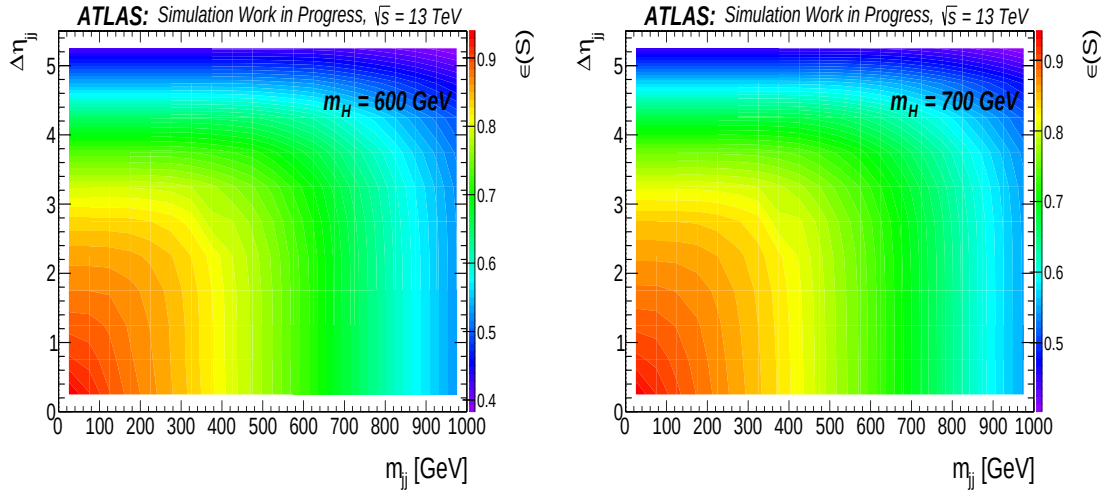

(a) (b)

Figure B.1: Selection efficiency maps for (a) $m_H = 600$ GeV and (b) $m_H = 700$ GeV mass points.

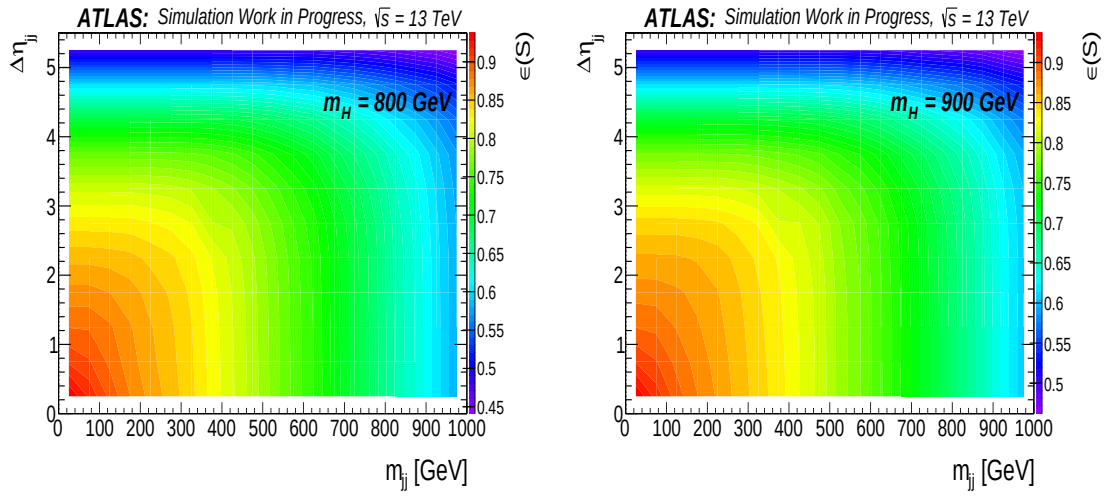

(a) (b)

Figure B.2: Selection efficiency maps for (a) m_H = 800 GeV and (b) m_H = 900 GeV mass points.

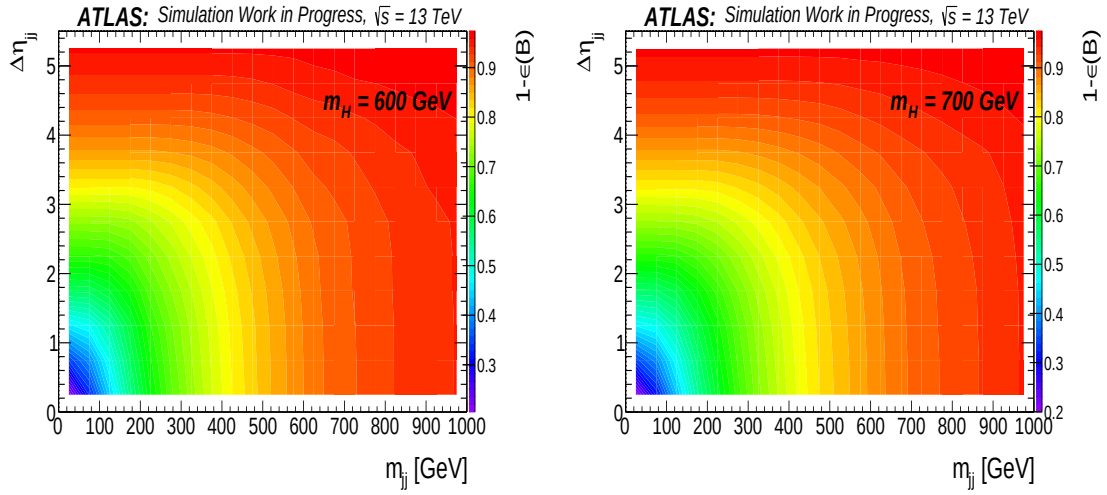

(a) (b)

Figure B.3: background rejection maps for the (a) m_H = 600 GeV and (b) m_H = 700 GeV mass points.

In order to select clean signal events, the ability of the applied selection method to reject unwanted events is important. Background rejection shows the fraction of events that are removed after each set of selection requirements is applied. The background rejection is shown in figure B.3 for the 600 GeV and 700 GeV mass points and figure B.4 for the 800 GeV and 900 GeV mass points.

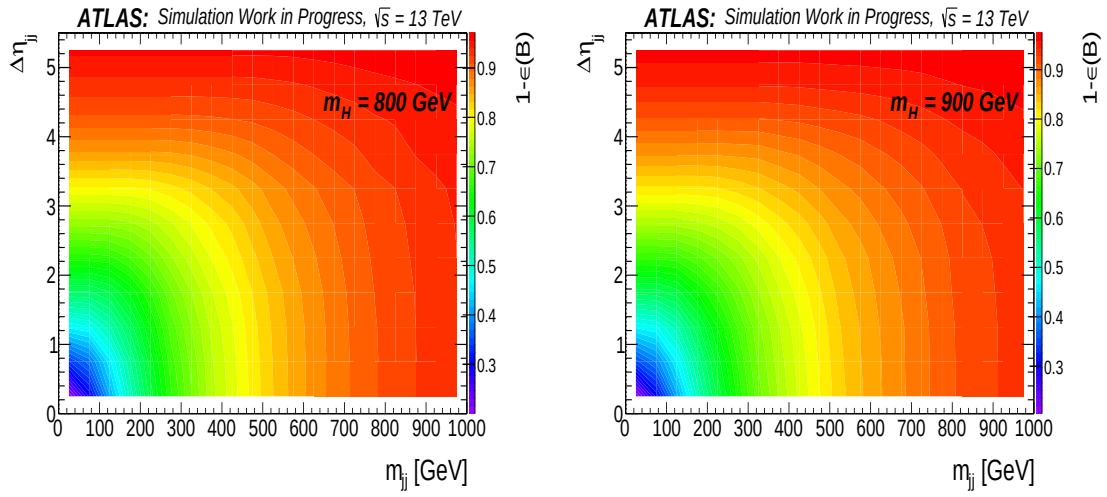

(a) (b)

Figure B.4: background rejection maps for the (a) m_H = 800 GeV and (b) m_H = 900 GeV mass points.

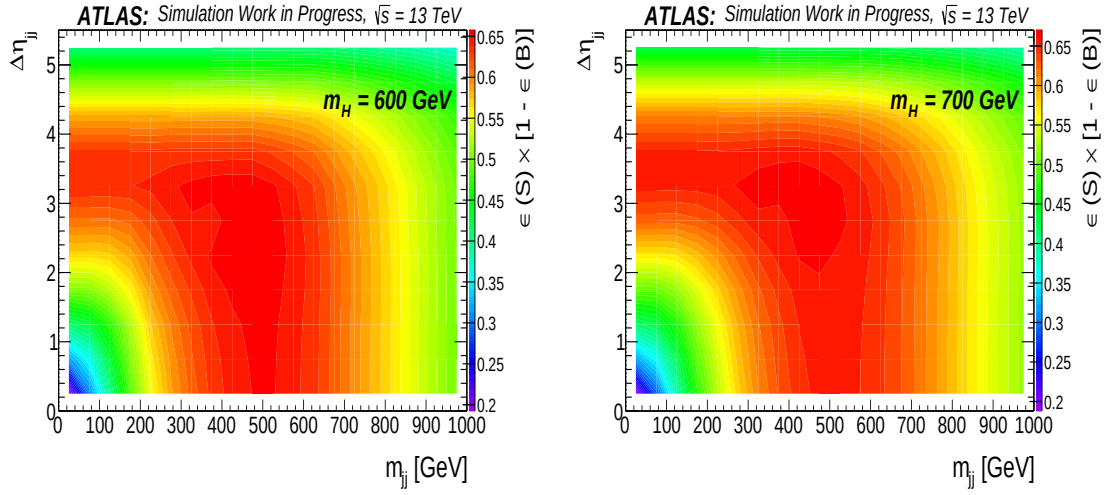

(a) (b)

Figure B.5: ϵ(S) × [1- ϵ(B)] maps for the (a) m_H = 600 GeV and (b) m_H = 700 GeV mass points.

To optimize the signal selection for each sample mass point, a product of signal selection efficiency and background rejection is calculated after each set of cuts is applied. This is shown in figure B.5 for the m_H = 600 GeV and m_H = 700 GeV mass points and figure B.6 for the m_H = 800 GeV and m_H = 900 GeV mass points. Each of these figures provides the optimal signal selection cuts for the respective mass point which are obtained by getting the largest value of ϵ(S) × [1- ϵ(B)]. The overall

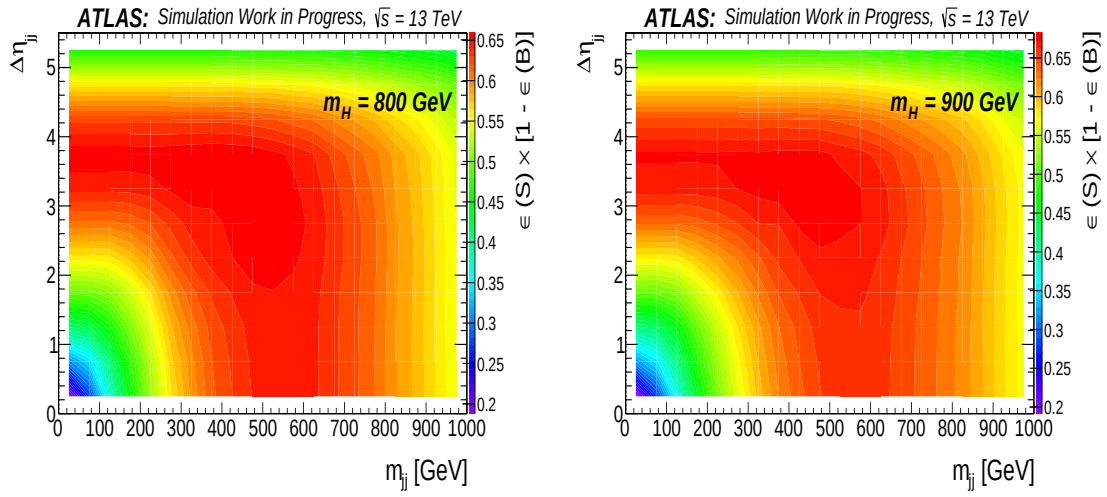

(a) (b)

Figure B.6: ϵ(S) $\times$ [1- ϵ(B)] maps for the (a) m_H = 800 GeV and (b) m_H = 900 GeV mass points.

cut value that can be applied on all samples was obtained by summing all ϵ(S) $\times$ [1- ϵ(B)] and finding the maximum or by taking the average of the obtained cut values over all sample mass points in the range considered as explained in chapter 5.

B.2 DNN-based Classifier

To improve the separation of the VBF category from the non-VBF category and the search sensitivity of the VBF signal, a Machine Learning technique to use for event categorization has been developed. This is a multivariate classifier called the deep neural network (DNN). Before the DNN classifier is trained, the standard event selection as introduced in section 4.4 has to be applied to all events. The DNN is constructed with three parts: one multi-layer perceptron (MLP) [63, 64] and two recurrent neural networks (RNN) [65, 66]. The classifier is trained on VBF signal samples and ZZ background using the input features summarized in table B.1 and table B.2. A total of 1.1 million background events and 0.3 million signal events were used to train the DNN classifier. During training, the VBF signal is used and signal events are re-weighted to match the background $m_{4\ell}$ spectrum. The kinematic variables of leptons and jets are used as input features for the network. There are nine input features used for the VBF-DNN classifier and twelve features for the ggF-DNN classifier. The input features to the VBF-DNN are summarized in table B.1 and the input variables for the ggF-DNN are shown in table B.2.

Table B.1: Input variables in the VBF-DNN classifier

feature	**description**
$m_{4\ell}$	four lepton invariant mass
m_{jj}	dijet invariant mass
p_T^{jj}	dijet transverse momentum
η^j	pseudo-rapidities of two leading jets
$\Delta\eta_{jH}$	pseudo-rapidity difference between a lading jet and the four lepton system
$\min\Delta R_{Zj}$	minimum angular separation between a lepton pair and a jet
p_T^j	transverse momenta of two leading jets
p_T^ℓ	transverse momenta of the four leptons
η^ℓ	pseudo-rapidities of the four leptons

Table B.2: Input variables in the ggF-DNN classifier

feature	**description**
$m_{4\ell}$	four lepton invariant mass
$\cos\theta_1$	decay angle of a leading Z boson
$\cos\theta_2$	decay angle of a sub-leading Z boson
$\cos\theta^*$	production angle of the ZZ system
$p_T^{4\ell}$	transverse momentum of the 4ℓ system
$\eta^{4\ell}$	pseudo-rapidity of the four-lepton system
ϕ	azimuthal angle of the ZZ system
ΔR_{jH}	angular separation between a leading jet and the 4ℓ system
p_T^j	transverse momentum of up to one jet
p_T^ℓ	transverse momenta of the four leptons
η^j	pseudo-rapidity of up to one jet
η^ℓ	pseudo-rapidities of the four leptons

As shown in table B.2, no dijet information was used in the training of a ggF-DNN classifier. A cut with good overall performance across all mass points and with high background rejection and high signal selection efficiency is chosen as the optimal cut for the classifier. Two sets of cuts were obtained: one for the VBF-DNN and one for the ggF-DNN. In the VBF category, events with two or more jets and VBF-DNN output score > 0.8 are selected. The ggF selection requires events with less than two jets and ggF-DNN output score > 0.5 or events with two or more jets

and VBF-DNN output score < 0.8. Details on this categorization method can be found in reference [2].

Bibliography

[1] B. M. Cano et al., "Search for heavy ZZ resonances in the $\ell^+\ell^-\ell^+\ell^-$ final state using proton–proton collisions at $\sqrt{s} = 13$ TeV with the ATLAS detector", Tech. rep. ATL-COM-PHYS-2018-1042. Geneva: CERN, (2018). url: https://cds.cern.ch/record/2630815.

[2] S. H. Abidi, C. Anastopoulos et al., "Searches for heavy Higgs bosons in the four-lepton decay channel with the ATLAS detector using 140 fb^{-1} of $\sqrt{s} = 13$ TeV data", Tech. rep. ATL-COM-PHYS-2018-1697. Geneva: CERN. (2018), url: https://cds.cern.ch/record/2650983.

[3] O. Mtintsilana, M. Thabede and T. Lagouri, "The ATLAS H4l Analysis Framework and the baseline analysis for the $H \to ZZ \to 4\ell$ channel", to appear in the book of proceedings of HEPP2018, Stellenbosch, 31 Jan - 02 Feb 2018.

[4] M. Thabede, B. Mellado, T. Lagouri and X. Ruan, "High mass VBF Categorization for Narrow-width Resonance searches in the $H \to ZZ \to 4\ell$ channel with the ATLAS detector", to appear in the book of proceedings of SAIP2019, Polokwane, 8-12 July 2019.

[5] G. Aad et al., "Observation of a new particle in the search for the Standard Model Higgs boson with the ATLAS detector at the LHC", In:*Phys. Lett.* **B716** (2012), p. 1-29. doi: 10.1016/j.physletb.2012.08.020, arxiv:1207.7214 [hep-ex].

[6] S. Chatrchyan et al., "Observation of a New Boson at a Mass of 125 GeV with the CMS Experiment at the LHC", In:*Phys. Lett.* **B716** (2012), p. 30-61. doi: 10.1016/j.physletb.2012.08.021, arxiv:1207.7235 [hep-ex].

[7] C. Curceanu et al., "Test of the Pauli Exclusion Principle in the VIP-2 underground experiment", In:*Entropy* **19.7** (2017), p. 300. doi: 10.3390/e19070300, arxiv:1705.02165 [quant-ph].

[8] **CMS** Collaboration, "Measurement of the top-quark mass in t t-bar events with lepton+jets final states in pp collisions at sqrt(s)=8 TeV", Tech. rep. CMS-PAS-TOP-14-001. Geneva: CERN, 2014. url: https://cds.cern.ch/record/1690093.

[9] A. Coley, "Mathematical General Relativity", In: *Gen. Rel. Grav.* **51.6** (2019), p. 78. doi: 10.1007/s10714-019-2559-5, arxiv:1807.08628 [gr-qc].

[10] L. Heisenberg, "A systematic approach to generalisations of General Relativity and their cosmological implications", In:*Phys. Rept.* **796** (2019), p. 1-113. doi: 10.1016/j.physrep.2018.11.006, arxiv:1807.01725 [gr-qc].

[11] G. Ecker, "Quantum Chromodynamics", In: *High-energy physics. Proceedings, European School, Kitzbuehel, Austria, August 21-September, 2005* (2006), arxiv:hep-ph/0604165 [hep-ph].

[12] A. Grozin, "Quantum Chromodynamics", In: *Proceedings, 11th International Baikal Summer School on Physics of Elementary Particles and Astrophysics: Bolshie Koty, Irkutsk region, Russia, July 3-10, 2011* (2012). arxiv:1205.1815 [hep-ph].

[13] V. A. Bednyakov, N. D. Giokaris and A. V. Bednyakov, "On Higgs mass generation mechanism in the Standard Model", In:*Phys. Part. Nucl.* **39** (2008), p. 13-36. doi: 10.1007/s11496-008-1002-9, arxiv:hep-ph/0703280 [HEP-PH].

[14] A. Dobado, "Brout-Englert-Higgs mechanism for accelerating observers", In:*Phys. Rev.* **D96.8** (2017), p. 085009. doi: 10.1103/PhysRevD.96.085009, arxiv:1710.01564 [gr-qc].

[15] I. Sogami, "Generalized Covariant Derivative with Gauge and Higgs Fields in the Standard Model", In: *Progress of Theoretical Physics - PROG THEOR PHYS KYOTO* **94** (July 1995), pp. 117-123. doi: 10.1143/PTP.94.117.

[16] G. Bernardi and M. Herndon, "Standard model Higgs boson searches through the 125 GeV boson discovery", In: *Rev. Mod. Phys.* **86.2** (2014), p. 479. doi: 10.1103/RevModPhys.86.479, arxiv:1210.0021 [hep-ex].

[17] J. R. Andersen et al., "Handbook of LHC Higgs Cross Sections: 3. Higgs Properties", In: (2013), doi: 10.5170/CERN-2013-004, arxiv:1307.1347 [hep-ph].

[18] S. Buddenbrock, N. Chakrabarty, A. S. Cornell, D. Kar, M. Kumar, T. Mandal, B. Mellado, B. Mukhopadhyaya and R. G. Reed, "The compatibility of LHC Run 1 data with a heavy scalar of mass around 270 GeV", In: (2015), p. . doi: , arxiv:1506.00612 [hep-ph].

[19] S. Buddenbrock, N. Chakrabarty, A. S. Cornell, D. Kar, M. Kumar, T. Mandal, B. Mellado, B. Mukhopadhyaya, R. G. Reed and X. Ruan, "Phenomenological signatures of additional scalar bosons at the LHC", In: *Eur. Phys. J.* **C76.10** (2016), p. 580. doi: 10.1140/epjc/s10052-016-4435-8, arxiv:1606.01674 [hep-ph].

[20] S. Buddenbrock, A. S. Cornell, M. Kumar and B. Mellado, "The Madala hypothesis with Run 1 and 2 data at the LHC", In: *J. Phys. Conf. Ser.* **889.1** (2017), p. 012020. doi: 10.1088/1742-6596/889/1/012020, arxiv:1709.09419 [hep-ph].

[21] G. Aad et al., "Measurements of fiducial and differential cross sections for Higgs boson production in the diphoton decay channel at $\sqrt{s} = 8$ TeV with ATLAS", In: *JHEP* **09** (2014), p. 112. doi: 10.1007/JHEP09(2014)112, arxiv:1407.4222 [hep-ex].

[22] G. Aad et al., "Fiducial and differential cross sections of Higgs boson production measured in the four-lepton decay channel in *pp* collisions at $\sqrt{s}$=8 TeV with the ATLAS detector", In: *Phys. Lett.* **B738** (2014), p. 234-253. doi: 10.1016/j.physletb.2014.09.054, arxiv:1408.3226 [hep-ex].

[23] V. Khachatryan et al., "Measurement of differential cross sections for Higgs boson production in the diphoton decay channel in pp collisions at $\sqrt{s} = 8$ TeV", In: *Eur. Phys. J.* **C76.1** (2016), p. 13. doi: 10.1140/epjc/s10052-015-3853-3, arxiv:1508.07819 [hep-ex].

[24] V. Khachatryan et al., "Measurement of differential and integrated fiducial cross sections for Higgs boson production in the four-lepton decay channel in pp collisions at $\sqrt{s} = 7$ and 8 TeV", In: *JHEP* **04** (2016), p. 005. doi: 10.1007/JHEP04(2016)005, arxiv:1512.08377[hep-ex].

[25] G. Aad et al., "Searches for Higgs boson pair production in the $hh \to bb\tau\tau, \gamma\gamma WW^*, \gamma\gamma bb, bbbb$ channels with the ATLAS detector", In: *Phys. Rev.* **D92** (2015), p. 092004. doi: 10.1103/PhysRevD.92.092004, arxiv:1509.04670 [hep-ex].

[26] V. Khachatryan et al., "Search for two Higgs bosons in final states containing two photons and two bottom quarks in proton-proton collisions at 8 TeV", In: *Phys. Rev.* **D94.5** (2016), p. 052012. doi: 10.1103/PhysRevD.94.052012, arxiv:1603.06896 [hep-ex].

[27] V. Khachatryan et al., "Searches for a heavy scalar boson H decaying to a pair of 125 GeV Higgs bosons hh or for a heavy pseudo-scalar boson A decaying to Zh, in the final states with $h \to \tau\tau$", In: *Phys. Lett.* **B755** (2016), p. 217-244. doi: 10.1016/j.physletb.2016.01.056, arxiv:1510.01181 [hep-ex].

[28] V. Khachatryan, A. M. Sirunyan et al., "Searches for heavy Higgs bosons in two-Higgs-doublet models and for $t \to ch$ decay using multilepton and diphoton final states in pp collisions at 8 TeV", In: *Phys. Rev. D* **90** (2014), p. 112013. doi: 10.1103/PhysRevD.90.112013, url: https://link.aps.org/doi/10.1103/PhysRevD.90.112013.

[29] G. Aad et al., "Search for $H \to \gamma\gamma$ produced in association with top quarks and constraints on the Yukawa coupling between the top quark and the Higgs boson using data taken at 7 TeV and 8 TeV with the ATLAS detector", In: *Phys. Lett.* **B740** (2015), p. 222-242. doi: 10.1016/j.physletb.2014.11.049, arxiv:1409.3122 [hep-ex].

[30] G. Aad et al., "Search for the associated production of the Higgs boson with a top quark pair in multilepton final states with the ATLAS detector", In: *Phys. Lett.* **B749** (2015), p. 519-541. doi: 10.1016/j.physletb.2015.07.079, arxiv:1506.05988 [hep-ex].

[31] G. Aad et al., "Search for the Standard Model Higgs boson produced in association with top quarks and decaying into $b\bar{b}$ in pp collisions at $\sqrt{s} = 8$ TeV with the ATLAS detector", In: *Eur. Phys. J.* **C75.7** (2015), p. 349. doi: 10.1140/epjc/s10052-015-3543-1, arxiv:1503.05066 [hep-ex].

[32] V. Khachatryan et al., "Search for the associated production of the Higgs boson with a top-quark pair", In: *JHEP* **09** (2014), p. 087. doi: 10.1007/JHEP09(2014)087,10.1007/JHEP10(2014)106, arxiv:1408.1682 [hep-ex].

[33] G. Aad et al., "Search for a high-mass Higgs boson decaying to a W boson pair in pp collisions at $\sqrt{s} = 8$ TeV with the ATLAS detector", In: *JHEP* **01** (2016), p. 032. doi: 10.1007/JHEP01(2016)032, arxiv:1509.00389 [hep-ex].

[34] G.Aad et al., "Search for an additional, heavy Higgs boson in the $H \to ZZ$ decay channel at $\sqrt{s} = 8$ TeV in pp collision data with the ATLAS detector", In: *Eur. Phys. J.* **C76.1** (2016), p. 45. doi: 10.1140/epjc/s10052-015-3820-z, arxiv:1507.05930 [hep-ex].

[35] V. Khachatryan et al., "Search for a Higgs boson in the mass range from 145 to 1000 GeV decaying to a pair of W or Z bosons", In: *JHEP* **10** (2015), p. 144. doi: 10.1007/JHEP10(2015)144, arxiv:1504.00936 [hep-ex].

[36] S. Buddenbrock, A. S. Cornell, Y. Fang, A. Fadol Mohammed, M. Kumar, B. Mellado and K. G. Tomiwa, "The emergence of multi-lepton anomalies at the LHC and their compatibility with new physics at the EW scale", In: *JHEP* **10** (2019), p. 157. doi: 10.1007/JHEP10(2019)157, arxiv:1901.05300 [hep-ph].

[37] P. Rapheeha, "Compatibility of a simplified BSM model with the observed excesses in multiple lepton production at the LHC", to appear in the book of proceedings of SAIP2019, Polokwane, 8-12 July 2019.

[38] O. Brandt, "Search for Supersymmetry in Trilepton Final States with the ATLAS Detector and the Alignment of the ATLAS Silicon Tracker", In: *Oxford U.* (2009), arxiv:1001.1365 [hep-ex].

[39] **ATLAS** Collaboration, "Track Reconstruction Performance of the ATLAS Inner Detector at $\sqrt{s} = 13$ TeV", Tech. rep. ATL-PHYS-PUB-2015-018 (2015), url: https://cds.cern.ch/record/2037683.

[40] M. Capeans, G. Darbo, K. Einsweiller, M. Elsing et al., "ATLAS Insertable B-Layer Technical Design Report", Tech. rep. CERN-LHCC-2010-013. ATLAS-TDR-19 (2010), url: https://cds.cern.ch/record/1291633.

[41] A. Vogel, "ATLAS Transition Radiation Tracker (TRT): Straw Tube Gaseous Detectors at High Rates", Tech. rep. ATL-INDET-PROC-2013-005. Geneva: CERN, (2013). url: http://cds.cern.ch/record/1537991.

[42] M. Aleksa and M. Diemoz, "Discussion on the electromagnetic calorimeters of ATLAS and CMS", Tech. rep. ATL-LARG-PROC-2013-002. Geneva: CERN, (2013), url: https://cds.cern.ch/record/1547314.

[43] **ATLAS** Collaboration, "ATLAS tile calorimeter: Technical Design Report", In: *Technical Design Report ATLAS* CERN-LHCC-96-042. (1996), url: http://cds.cern.ch/record/331062.

[44] J. T. Shank, "The ATLAS Detector: Status and Results from Cosmic Rays", In: *Particles and fields. Proceedings, Meeting of the Division of the American Physical Society, DPF 2009, Detroit, USA, July 26-31, 2009* (2009), arxiv:0910.3081 [hep-ex].

[45] **ATLAS** Collaboration, "Technical Design Report for the Phase-II Upgrade of the ATLAS Muon Spectrometer", Tech. rep. CERN-LHCC-2017-017. ATLAS-TDR-026. Geneva: CERN, (2017), url: https://cds.cern.ch/record/2285580.

[46] P. Nason and G. Zanderighi, "W^+W^- , WZ and ZZ production in the POWHEG-BOX-V2", In: *Eur. Phys. J.* **C74.1** (2014), p. 2702. doi: 10.1140/epjc/s10052-013-2702-5, arxiv:1311.1365 [hep-ph].

[47] T. Sjostrand et al., "A Brief Introduction to PYTHIA 8.1", In: *Comput. Phys. Commun.* **178** (2008), p. 852.867. doi: 10.1016/j.cpc.2008.01.036, arxiv:0710.3820 [hep-ph].

[48] R. D. Ball et al., "Parton distributions with LHC data", In: *Nucl. Phys.* **B867** (2013), p. 244-289. doi: 10.1016/j.nuclphysb.2012.10.003, arxiv:1207.1303 [hep-ph].

[49] H. Lai, M. Guzzi et al., "New parton distributions for collider physics", In: *Phys. Rev.* **D82** (2010), p. 074024. doi: 10.1103/PhysRevD.82.074024, arxiv:1007.2241 [hep-ph].

[50] T. Gleisberg, S. Höche et al., "Event generation with SHERPA 1.1", In: *Journal of High Energy Physics* (2009), p. 007–007. doi: 10.1088/1126-6708/2009/02/007.

[51] R. D. Ball, V. Bertone, S. Carrazza et al., "Parton distributions for the LHC run II", In: *Journal of High Energy Physics***2015** (2015), p. 40. doi: 10.1007/JHEP04(2015)040, url: https://doi.org/10.1007/JHEP04(2015)040.

[52] C. Matteo, P. S. Gavin and S. Gregory, "The anti-ktjet clustering algorithm", In: *Journal of High Energy Physics* **2008** (2008), p. 063–063. doi: 10.1088/1126-6708/2008/04/063.

[53] P. Achard, O. Adriani et al., "Measurement of the Z-boson mass using e+e$\rightarrow$ Z events at centre-of-mass energies above the Z pole", In: *Physics Letters B* **585** (2004), p. 42-52. doi: https://doi.org/10.1016/j.physletb.2004.01.074.

[54] I. Caprini et al., "Fiducial and differential cross sections of Higgs boson production measured in the four-lepton decay channel in pp collisions at $\sqrt{s} =$ 8 TeV with the ATLAS detector", In: *Physics Letters B* **738** (2014), doi: 10.1016/j.physletb.2014.09.054.

[55] M. Aaboud et al., "Measurement of inclusive and differential cross sections in the $H \to ZZ^* \to 4\ell$ decay channel in pp collisions at $\sqrt{s} = 13$ TeV with the ATLAS detector", In: *JHEP* **10** (2017), p. 132. doi: 10.1007/JHEP10(2017)132, arxiv:1708.02810 [hep-ex].

[56] A. M. Sirunyan et al., "Measurements of properties of the Higgs boson decaying into the four-lepton final state in pp collisions at $\sqrt{s} = 13$ TeV", In: *JHEP* **11** (2017), p. 047. doi: 10.1007/JHEP11(2017)047, arxiv:1706.09936 [hep-ex].

[57] Z. Marshall, "Simulation of Pile-up in the ATLAS Experiment", In: *Journal of Physics: Conference Series* **513** (2014), p. 022024. doi: 10.1088/1742-6596/513/2/022024.

[58] D. Cireşan, U. Meier, J. Masci and J. Schmidhuber, "Multi-column deep neural network for traffic sign classification", In: *Neural Networks* **32** (2012), p. 333-338. doi: https://doi.org/10.1016/j.neunet.2012.02.023, url: http://www.sciencedirect.com/science/article/pii/S0893608012000524.

[59] H. Mohsen et al., "Classification using deep learning neural networks for brain tumors", In: *Future Computing and Informatics Journal* **3** (2018), p. 68-71. doi: https://doi.org/10.1016/j.fcij.2017.12.001, url: http://www.sciencedirect.com/science/article/pii/S2314728817300636.

[60] B. P. Roe et al., "Boosted decision trees, an alternative to artificial neural networks", In: *Nucl. Instrum. Meth.* **A543** (2005), p. 577-584. doi: 10.1016/j.nima.2004.12.018, arxiv:physics/0408124 [physics].

[61] Y. Coadou, "Boosted Decision Trees and Applications", In: *EPJ Web Conf.* **55** (2013), p. 02004. doi: 10.1051/epjconf/20135502004.

[62] S. H. Abidi, "Run II Analysis Framework and Intial Validation Studies for $H \to ZZ^* \to 4\ell$ Analysis", Tech. rep. CERN-THESIS-2015-051. (2015), url: http://cds.cern.ch/record/2019782.

[63] D. Chen and W. J. Wang, "classification of wavelet map patterns using multilayer neural networks for gear fault detection", In: *Mechanical Systems and Signal Processing* **16** (2002), p. 695-704. doi: https://doi.org/10.1006/

mssp.2002.1488, url: http://www.sciencedirect.com/science/article/pii/S0888327002914883.

[64] M. W. Gardner and S. R. Dorling, "Artificial neural networks (the multilayer perceptron)—a review of applications in the atmospheric sciences", In: *Atmospheric Environment* **32** (1998), p. 2627-2636. doi: https://doi.org/10.1016/S1352-2310(97)00447-0, url: http://www.sciencedirect.com/science/article/pii/S1352231097004470.

[65] A. Sherstinsky, "Fundamentals of Recurrent Neural Network (RNN) and Long Short-Term Memory (LSTM) Network", In: *CoRR* **abs/1808.03314** (2018), arxiv:1808.03314, url: http://arxiv.org/abs/1808.03314.

[66] J. Kumar et al., "Long Short Term Memory Recurrent Neural Network (LSTM-RNN) Based Workload Forecasting Model For Cloud Datacenters", In: *Procedia Computer Science* **125** (2018), p. 676-682. doi: https://doi.org/10.1016/j.procs.2017.12.087, url: http://www.sciencedirect.com/science/article/pii/S1877050917328557.